UNIVERSITÀ DEGLI STUDI DI NAPOLI ‘‘FEDERICO II’’

SCUOLA POLITECNICA E DELLE SCIENZE DI BASE

Dipartimento di Ingegneria Chimica, dei Materiali e della Produzione Industriale

PhD thesis

in

INGEGNERIA DEI PROCESSI E PRODOTTI INDUSTRIALI

XXXI CICLO

ELECTROSTATIC SCRUBBING OF SUBMICRON PARTICLES: EXPERIMENTAL AND MODELING

Advisor board

Prof. Amedeo Lancia

Prof. Francesco Di Natale

Ing. Matteo Giavazzi

Doctoral Candidate

Martina Esposito

Summary

4.3.1 Particle capture tests *82*
4.3.2 Influence of operating parameters *87*
4.3.3 Comparison between Experimental and Modeled efficiency *89*
Conclusions ***92***
Bibliography ... ...

List of Symbols

A_b	WES bottom area
A_f	facet surface
$Area_{column}$	WES column area
b	collision parameter
B	magnetic field
b_{ion}	ion mobility
$C_{1\varepsilon}$	constant of the turbulent model
$C_{2\varepsilon}$	constant of the turbulent model
C_c	Cunningham factor
C_D	drag coefficient
c_i	gas mean speed
c_p	specific heat
$C\eta$	constant of the turbulent model
D	droplet diameter
d	electrode distance
D	is the rate deformation
D_{BR}	Particle Brownian diffusivity
Dc	duct diameter
d_p	particle diameter
E	electric field
e	electron charge
E_{BD}	Collision efficiency due to Brownian diffusion
E_{DI}	Collision efficiency due to directional interception
E_{Dph}	Collision efficiency due to diffusiophoresis
E_{Es}	Collision efficiency due to electrostatic attraction

E_{In}	Collision efficiency due to inertial impaction
E_{Peek}	Peek saturation field value
E_{Th}	Collision efficiency due to thermophoresis
E_{tot}	total collisional efficiency
F	generic term of the forces acting on the fluid
f	roughness coefficient
F_D	drag force
F_e	electric force
f_h	humidity correction factor
F_i	Termophoretic force
F_p	pressure force
F_v	viscous force
F_z	WES z-axis force
h_a	absolute humidity
i_{e0}	current carried by initial ions
i_{ea}	current carried by ions when the avalanche reaches the anode
I_{gen}	current supplied by generator
J	current density
k_B	Boltzmann's constant
K_c	Coulomb constant
k_g	Gas thermal conductivity
Kn	Knudsen number
n (d_p)	particle concentration
N	number of droplets
n_{e0}	number of initial ions
n_{ex}	number of ions per cm

N_i	mean ion concentration in the electric field in the charging unit
P	gas pressure
P_b	pressure at the bottom of reactor
q:	particle charge
q_{diff}	diffusion charge
q_{field}	field charge
q_r	Rayleigh limit
q_s	saturation limit charge
Q_{surf}	gas flow integral on a surface
r	scavenging rate
Re	Reynolds number
R_g	specific gas constant
RH	Relative humidity
r_p	particle radius
r_p	particle radius
r_w	wire radius
Sc	Particle Schmidt number
Sh	source term of energy
St	Stokes number
*St**	Critical Stokes number in Slinn equation
T	temperature
t_r	particle residence time in PCU
U	particle-droplet relative velocity
u_p	particle velocity
v	fluid velocity
V	voltage

V_0	onset Corona
V_b	breakdown voltage
v_{cell}	Eulerian velocity of the particles
Zi	ion mobility

Greek symbols

α	*Townsend first coefficient*
α'	Water packing factor – Jung and Lee model
β	Townsend second coefficient
γ	Townsend third coefficient
Γ_w	water surface tension
δ	sphere of influence radius according to Fuchs' radius
ε	Air dielectric constant
ε_0	vacuum permittivity
ε_r	relative permittivity
η	particle capture efficiency (per particle size)
η_t	is the eddy viscosity
η_{tot}	total particle capture efficiency
μ	Gas viscosity
μ_w	Water viscosity
$\overline{\lambda_e}$	electron mean free path
λ	mean free path
$\Lambda\ (d_p)$	scavenging coefficient
$\lambda\ (d_p)$	scavenging coefficient per number for number of droplets;

ρ	gas density
ρ_c	charge density
ρ_{ion}	ion concentration
ρ_p	particle density
ρ_w	water density
τ	particle saturation charging time in PCU
ψ	collision probability
$\psi(D)$	Droplet size distribution
$\psi(d_p)$	particle size distribution

List of Figures

List of Tables

Chapter 1. Introduction

It was proved that particle matter is associated with health disease, regarding at respiratory and cardiovascular illness. Ultrafine particles are the most hazardous fraction of dust: travelling long distances from the emitting source, they can remain in atmosphere [1] for a long time and once inhaled, can reach the deepest regions of the lungs and enter in the circulatory system [2].

The conventional particle abatement systems are not able to treat particles with sizes above or around 1µm, and they are far less effective towards the submicronic dimensions. Among the treatment devices, Wet Scrubbers (WS) are used in order to capture both particles and gaseous pollutants, but they are inefficient for particles in sub-micron range. It was demonstrated by Penney [3] that the presence of electrical charge on particles and droplets increases the capture efficiency, due the coulomb forces. These considerations lead to the concept of Wet Electrostatic Scrubber (WES), an upgrade of common WS, aimed to the capture of fine and ultrafine particles.

WES is made up of three main components:

- Particle Charging Unit: through a corona source particles gain electric charges on their surface. Several mechanism influence charging phenomena, but since corona discharge is a complex phenomenon thus depends on different unpredictable variables, as uninform electric field, particle shape and particle residence time in the charging device;
- Electrified spray: water droplets are electrically charged through an induction system. The complexity linked to the fluid dynamic of sprayed droplets is not described deeply in this work, but it is largely explained in literature;
- Contact Chamber: where gaseous flow, containing charged particles, and liquid droplets enter in contact and through several mechanisms, fine dusts are removed by water drops. The contact between the two phases might be co-current or crossflow, depending on the fluid dynamic of the system and on residence time, both for gas flow, i.e. particles, and for droplets.

Different experimental investigations confirmed WES ability to increase the particle capture efficiency compared to WS units, but its optimization is still an unsolved problem as many variables are involved in the collection mechanism.

1.1 Particle matter

Several natural and anthropogenic processes produce relevant quantity of solid and liquid pollutants, which are released in atmosphere. The combination of these compounds composes the *particulate matter*. An idealized distribution of particulate matter in ambient air is shown in *Figure 1-1*.

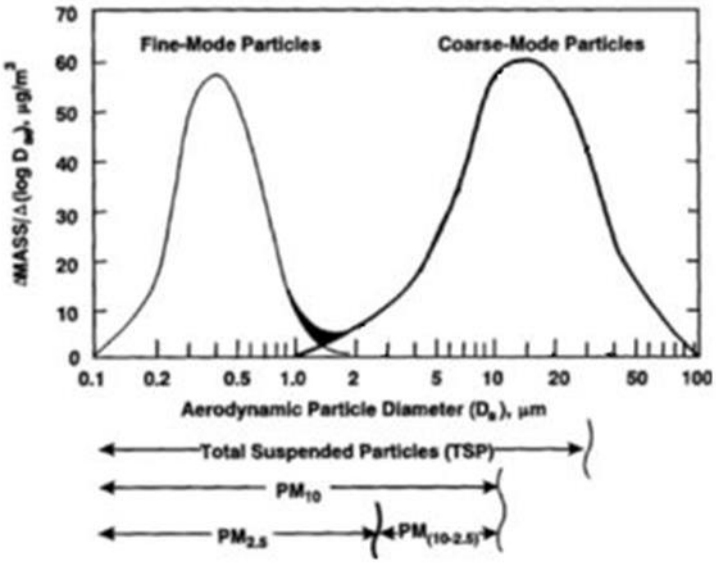

Figure 1-1 Different categories of particle matter

Particulate matter varies in size, composition and origin; it is essentially divided in four categories, depending on the particle dimension:

- ***Coarse (2-100 µm)***: This function results from natural processes, such as erosion, desert and marine aerosols. The chemical composition is deeply influenced by the geographical area.
- ***Fine (0.1 µm and 1-2 µm):*** this fraction includes single particles, solid or obtained by volatiles condensation and by agglomerates od finer species, as soot.
- ***Ultrafine (10-100 nm):*** they usually derive from nucleation mechanism in combustion systems. They are basically composed by elementary and organic carbon.
- ***Nanoparticles (<10 nm):*** they compose the so called nucleation interval. These particles are macromolecules usually formed in flames or during gas discharges that behaves as condensed species and are the elemental bricks for the formation of ultrafine soot particles.

Several researches indicated that particles size plays an important role in defining toxicity as much as their chemical composition, which give rise to high surface reactivity and ability to cross cell membranes [2].

Emitted particles also affect climate. One important effect is that related to cloud formation, since they act as water condensation nuclei [1]. This role is actually more pronounced for sulphates. A fraction of the elemental carbon, known as black carbon (BC), has a mass absorption efficiency of 5 m^2/g at the wavelength of 550 nm, therefore it represents one of the most important climate warming agent after CO_2.

Among the most relevant industrial plants emission, there are cement plants, steel industries and power plants.

For cement process, the main sources of dust emission (*Table 1-1*) are raw material preparation process (raw mills), grinding and drying units, the clinker burning process (kiln and clinker coolers), the fuel and the cement grinding unit (mills).

Emissions source		Total dust concentration(1) (mg/Nm³)	Fine dust fraction (%)			Fine dust concentration (mg/Nm³)		
			< 2.5	< 10	> 10	< 2.5	< 10	> 10
			µm					
Kiln (ESP)(2)	Kiln flue-gas after ESP	15.4	51	87	13	7.9	13.4	2.9
Clinker cooler (ESP)	Clinker cooler flue-gas after ESP	14.0	68	99	1	9.5	13.9	≤ 0.1
Cyclone preheater (ESP), direct mode(3)	Kiln flue-gas after ESP	2.3	84	97	3	1.9	2.2	≤ 0.1
Cyclone preheater (ESP), combined mode(4)	Kiln flue-gas after ESP	4.8	66	97	3	3.2	4.7	≤ 0.1

(1) Total dust measured with filter sampler measurements (plane filter device), size segregation with cascade impactors
(2) Lepol kiln, now shut down
(3) Mill off
(4) Mill on
Source: [117, Germany, 2000]

Table 1-1 Investigation on fine dust distribution in total dust from German cement kilns[4]

In steel industries, the composition of the coarse dust is related to that of the sinter feed. The fraction of fine dust consists of alkali and lead chlorides formed during the sintering process itself. Quantitative analysis of grain size distribution of the dust from a sinter strand before abatement shows two maxima: one for coarse dust (with a grain size of about 100 µm) and one for PM_1 (0.1 – 1 µm) as reported in *Fig. 1-2* [5].

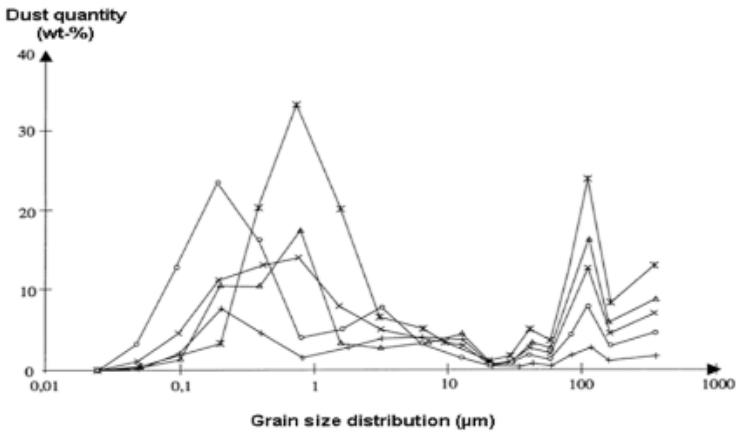

Figure 1-2 Grain size and weight distribution of dust from various sinter strands [5]

PM_{10} emissions to air are shown in *Figure 1-3* by industry sector. In 2014, 165 facilities in the "Thermal power stations and other combustion installations" sector emitted a total of 49 kt of PM_{10} emissions to air, representing 48.1 % of the total amount emitted [6].

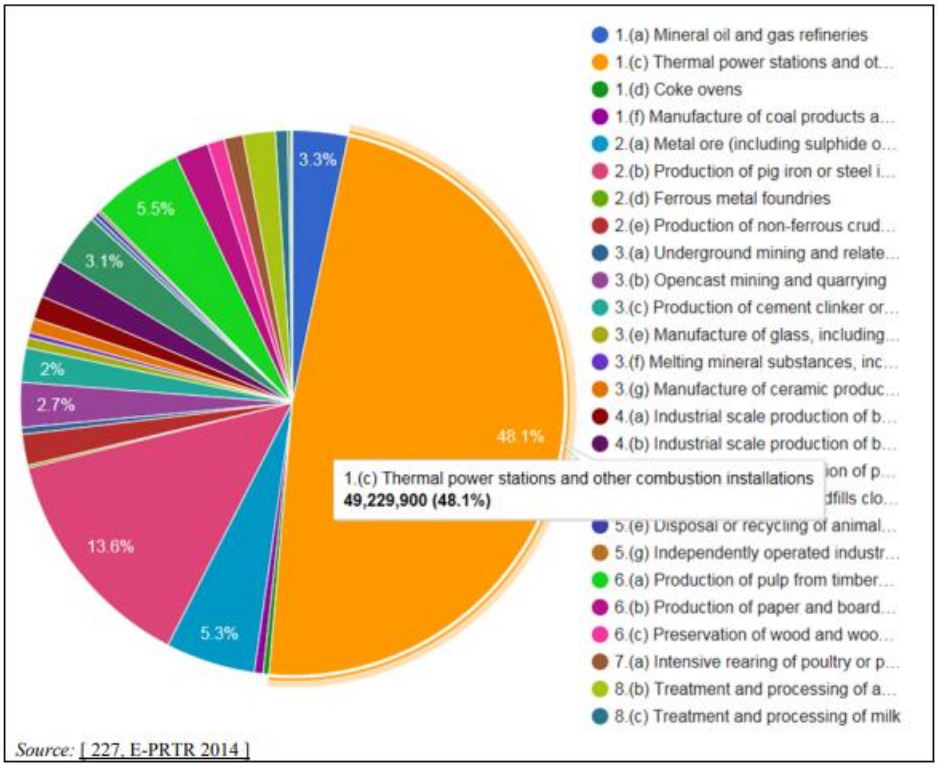

Figure 1-3 Emissions of PM_{10} to air by industry sector/activity in the EU-28 in 2014 [6]

Nowadays, the main systems used for particle abatement are based on inertial effects, filtration or electrical attractions and can be classified as:

- Cyclone: this system is based on inertial separation. Particles collide with the cyclone walls and then fall because of the gravity force;
- Scrubber: water droplets fall from the top of the scrubber and intercept the particle matter carried by a gas current.
- ESP: the abatement is due to the potential difference through the walls of the filters. Dust is electrically charged and get collected on the plates of the system, set to the ground potential.
- Fabric filters: dust laden gases enter the filter, where they meet a series of cylindrical bags (sleeves). The gas reaches speeds usually of the order of a few m / s. The material of which the sleeves consist is treated so as to have a permeability such as to pass the gas, but not dust, which adheres to them.

Conventional technologies present a lack in capture efficiency in the particle diameter range from 0.01 to 1µm, called *Greenfield gap* region (*Fig 1-4)*. Therefore, a new challenge of the scientific research is the development of new cleaning systems to remove particles from flue gas and the optimization of the existing technologies in order to improve the particle capture of submicronic particles, in particular in the Greenfield.

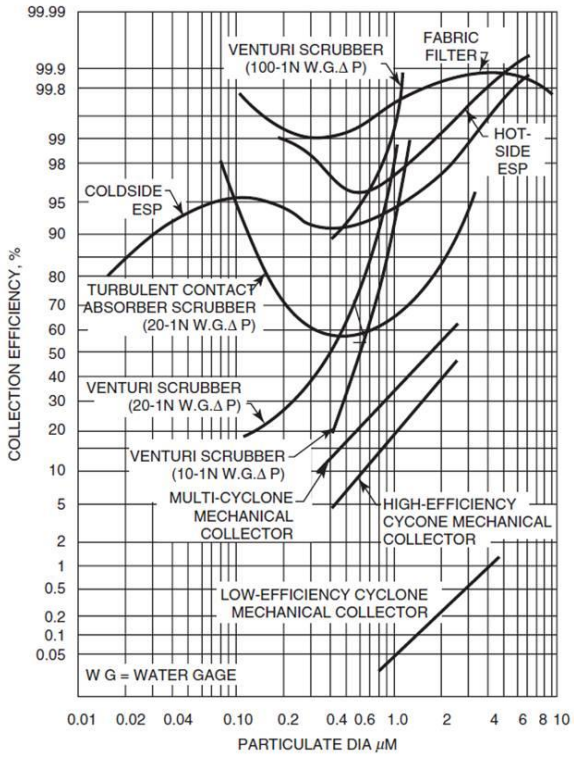

Figure 1-4: Comparison of removal efficiencies of different equipment as a function of particles diameter

Among the existing abatement systems, even though the collection (or abatement) efficiency is not high, wet scrubbers presents many advantages as the low pressure drops, the reduced process costs, the possibility to work at high temperature and the simultaneous ability to capture particles and gaseous pollutants (SOx, NOx , HCl, soluble VOCs).

Several studied were carried out on the wet scrubbers' upgrading by implementing the electrification of sprayed water and the particles in a gas stream resulting in electrodynamics interactions among particles and droplets.

The dust carried by a gas flow stream is captured in an empty column by charged water spray as those used for wet scrubbing. The wet electrostatic scrubber can be placed downstream a particle charging unit (PCU), where the gas stream is contacted with a corona source to charge the particles with polarity opposite to that of the spray.

Table 1-2 reports a survey of the existing PM_1 control techniques. Among them, only *wet electrostatic scrubbers, WES*, (wet or dry) electrostatic precipitators, ESP, fabric (FF) and HEPA filters, and Venturi scrubbers, VS, allow overcome 90% particle removal efficiency for PM_1. FF,

HEPA, ESP and VS reached full maturity in the last 10 years, and together with their performances their limitations were well assessed.

	FF*	ESP*	VS*	HEPA filters*	WES
Raccomanded for fine particles (<2.5µm)					
Application for ultra fine particles (<0.1µm)					
Appliation to bioaerosol	Yes	Yes	No	Yes	No
Pressure drop - kPa	0.5-50	0.05-0.5	2.5-20 (venturi)	0.05-0.25	0.5-1
Energy kWh/1000Nm^3	0.2-2	0.5-2	0.5-6	<0.1	≈0.2
Footprint					
Capital costs for 1000Nm^3/h	5300-50000USD	8500-18000USD	1900-17000USD	1800-2400USD	n.a
Sensibility to particle concentration					
Sensibility to particle stikiness/liquid aerosol					
Sensibility to particle resisitivity					
Risk for biological growth/offsprings					
Possibility of disinfection	No	No	Yes	No	Yes
Cross-media effects	Dust disposal	Disposal of dust	Waste-water disposal (Large)	Disposal of loaded filter modules	Waste-water disposal (small

Table 1-2 Comparison of conventional and innovative technologies for particle capture. BREF references. Data for WES and HC-WES from literature and personal know-how.

The WES systems are very effective, and have several advantages respect to FF and ESP. In particular:

- Allowing soluble gaseous pollutants removal;
- Almost insensitive to particle stickiness and electric resistivity,
- Having very low values of pressure drops, energy consumption and footprint.
- WES are not subjected to the risk of unwanted growth and offsprings of bacteria or fungi on their surfaces and may be developed also for high gas flow rates and particle concentration, differently from the HEPA filters.

One of the most challenging technological problem of WES is that the charging of particle finer than 200 nm (PM$_{<}$0.2) is quite difficult, since this process involves a charging mechanism (the diffusion charging) which is less effective than that observed for coarser particles (the field charging).

1.1.1 Wet Electrostatic Scrubber

Fig. 1-5 shows the operating principles of the WES system. Despite of the conventional scrubbers, with the WES technology high voltage is used to charge both particles and the liquid.

The WES unit consists in three main components:

1 Electrified spray;

2 Corona charging for particles;

3 The gas/spray contact chamber.

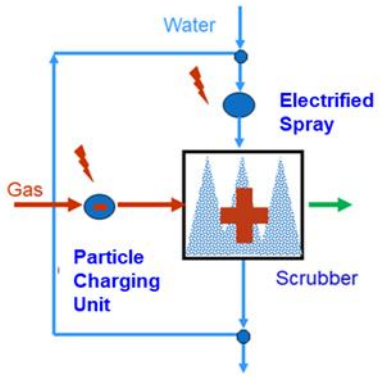

Figure 1-5 WES operating principle

Particles firstly pass through the *Particle Charging Unit (PCU)* made up of a series of needles connected to a high voltage generator. The charging process is due to the *corona effect*: the ionization of the gas that carries particles implies the acquirement of an electrical charge by particles themselves.

The electrified spray consists of a spray nozzle purposely charged by an induction charging.

The contact chamber is a spray tower usually co-current or crossflow. Particles, electrically charged in PCU device, enter in contact with liquid droplets charged with opposite polarity and because of Coulomb forces, they are captured by water.

1.1.2 Mathematical model for particle abatement

Di Natale et al. [7] proposed a mathematical model which describes the capture of particulate matter due to charged liquid droplets (*eq. 1-1*):

$$r(d_p, t) = n(d_p)\, x\, \frac{\pi}{4}\left[D(t) + d_p\right]^2 U(t)\, x\; E_{tot}(D(t), d_p) \qquad (1\text{-}1)$$

While a drop falls through a particle-laden gas, it collides with aerosol particles and can collect them. As the droplet falls, it sweeps (per unit time) the volume of a cylinder equal to $\pi D^2 U_d / 4$, where U_d, is its falling velocity and D its diameter. As a first approximation, one would be tempted to conclude that the droplet would collect all the particles that are in this volume. Actually, if the aerosol particles have a diameter d_p, a collision will occur if the center of the particle is inside the cylinder with diameter $D + d_p$. Also, the particles are moving with a velocity $u(d_p)$. So the "collision volume" per time becomes $\pi (D + d_p) 2 | U_d(D) - u(d_p)| / 4$, where $| U_d(D) - u(d_p)|$ is the relative velocity in the collision volume is valid when the particles flow is co-current with the falling droplets.

The total collision efficiency $E_{tot}(D, d_p)$ is commonly introduced to indicate the fraction of particles of diameter d_p contained within the collision volume of a drop with a diameter D that are actually collected. Thus E_{tot} (D, d_p) can be viewed as a correction factor accounting for the "active" interactions between the falling drop and the aerosol particle. If $n(d_p)$ is the concentration of the particle of diameter d_p, the number of active collisions between particles of this diameter and one drop of diameter D is shown in eq. *(1-2)*:

$$\frac{\pi}{4}\left(D + d_p\right)^2 \left|U_d(D) - u\left(d_p\right)\right| E_{tot}\left(D, d_p\right) n\left(d_p\right) \qquad (1\text{-}2)$$

When the entire ensemble of sprayed droplets is considered, the total rate of collection of all particles of diameter d_p is obtained integrating *eq. (1-2)* over the droplet number concentration and size distribution ψ(D) (eq. *1-3*):

$$n|_{d_p} = n\left(d_p\right) \int_0^\infty \frac{\pi}{4}\left(D + d_p\right)^2 \left|U_d(D) - u\left(d_p\right)\right| E_{tot}\left(D, d_p\right) \psi(D) N dD \qquad (1\text{-}3)$$

Where *N* is the total droplet concentration in the scrubber. The scavenging rate (*eq. 1-4*) of aerosol particles of diameter d_p can be written as:

$$\frac{dn(d_p)}{dt} = -\lambda\left(d_p\right) N\, n\left(d_p\right) \qquad (1\text{-}4)$$

With $\lambda(d_p)$ is the scavenging coefficient per number of droplets, therefore $\Lambda(d_p) = \lambda(d_p)\, N$ is called *scavenging coefficien*t and is the integral in the *eq. (1-3)* considering an initial value of particle

concentration $n(d_p, 0)$ as reported in *eq.* (*1-5*), that is obtained by the integration over the time t of the *eq.* (*1-4*) gives :

$$\boldsymbol{n}(d_p, t) = n(d_p, 0)e^{-\Lambda(d_p)t} \qquad (1\text{-}5)$$

Therefore, collection efficiency (*eq. 1-6*) for the particle diameter d_p, that remaining in the reactor for a time equal to t_p, can be written as:

$$\eta(d_p) = \frac{n(d_p,0) - n(d_p,t_c)}{n(d_p,0)} = 1 - e^{-\Lambda(d_p)t} \qquad (1\text{-}6)$$

The abatement model has been validated on laboratory scale [8] but there were difficulties on applying the capture model to a larger scale, because of the presence of other phenomena that are still unknown.

Collisional efficiency

The so-called collisional efficiency describes the forces originated from the interactions between falling droplets (the collectors) and particles and there are six major particle collection mechanisms of particle collection by water droplets each of which corresponds to a the effect of different physical phenomena and to a particular collisional efficiency. Three phenomena influence particle capture, described above.

In *Table 1-3* all the collisional mechanism are reported in detail.

- ***Hydrodynamic interation****:*
  - *Inertial Impact, E_{IN}*: the particles with a diameter minus than 10 μm are captured thanks to this phenomenon. The gas streamline diverges around the droplet, but the particle size is big enough to have its own inertia. This fact allows the particle to be intercepted by the droplet;
  - *Directional interception, E_{DI}*: for particle size smaller than 10 μm, the capture is due to the fact that particle strokes the droplet and then it's captured;
  - *Brownian Impact, E_{BD}*: This phenomenon is explained by the fact that the submicron particles and in particular those with diameter of smaller than 1 micron have a random path.

- ***Electrostatic interactions***, *E_{ES}*: Electrostatic attractions occur because the particle, the droplet, or both possess sufficient electrical charge to overcome the inertial forces; than the particle can be attracted by the droplet and collected. If only droplets or particles are charge, the electrostatic forces are also present due to image forces.
- ***Phoretic interactions****:*
  - *Thermophoresis, E_{Th}*: it has a positive effect on particle capture, in fact the gas thermal gradient moves the particle to the droplet, because the impact is easier where temperature is higher;
  - *Diffusiophoresis, E_{Dph}*: its contribution is negative. The droplet evaporation due to the high temperature, causing a concentration gradient, push the particle away

-

INERTIAL IMPACTION, E_{In}

$$E_{In} = \left[\frac{St - St^*}{St - St^* + 2/3}\right]^{\frac{3}{2}} \left(\frac{\rho_p}{\rho_w}\right)^{\frac{1}{2}} \quad (1\text{-}7)$$

$$St = \frac{C_c \rho_p d_p^{\,2} U}{18 \mu D} \quad (1\text{-}8) \qquad [9]$$

$$St^* = \frac{1/2 + 1/12 \cdot \ln[1 + \mathrm{Re}]}{1 + \ln[1 + \mathrm{Re}]} \quad (1\text{-}9)$$

$$E_{In} = \left[\frac{St}{St + 0.35}\right]^2 \quad (1\text{-}10) \qquad [10]$$

$$E_{In} = 3.4 St^{\frac{3}{2}} \quad \text{at} \quad St \le 0.5$$
$$E_{In} = 1 \quad \text{at} \quad St > 0.5 \quad (1\text{-}11) \qquad [11]$$

DIRECTIONAL INTERCEPTION, E_{DI}

$$E_{DI} = 4H\left[\omega^{-1} + (1 + 2\mathrm{Re}^{1/2})H\right] \quad (1\text{-}12)$$

$$\omega = \frac{\mu_w}{\mu} \quad (1\text{-}13) \qquad [9]$$

$$H = \frac{d_p}{D} \quad (1\text{-}14)$$

$$E_{DI} = \frac{(1 - \alpha')}{(J + \omega K)}\left[\left(\frac{H}{1+H}\right) + \frac{1}{2}\left(\frac{H}{1+H}\right)^2 (3\omega + 4)\right] \quad (1\text{-}15)$$

$$J = 1 - \frac{6}{5}\alpha'^{\frac{1}{3}} + \frac{1}{5}\alpha'^2 \quad (1\text{-}16)$$

$$\omega = \frac{\mu_w}{\mu} \quad (1\text{-}17) \qquad [12]$$

$$K = 1 - \frac{9}{5}\alpha'^{\frac{1}{3}} + \alpha + \frac{1}{5}\alpha'^2 \quad (1\text{-}18)$$

$$H = \frac{d_p}{D} \quad (1\text{-}19)$$

BROWNIAN DIFFUSION, E_{BD}

$$E_{BD} = \frac{4}{\mathrm{Re}\, Sc}\left[1 + 0.4\mathrm{Re}^{\frac{1}{2}} Sc^{\frac{1}{3}} + 0.16\,\mathrm{Re}^{\frac{1}{2}} Sc^{\frac{1}{2}}\right] \quad (1\text{-}20) \qquad [9]$$

$$Sc = \frac{\mu}{\rho D_{BR}} \qquad (1\text{-}21)$$

$$D_{BR} = \frac{k_B C_c T}{3\pi \mu d_p} \qquad (1\text{-}22)$$

ELECTROSTATIC INTERACTIONS, E_{Es}			
$E_{Es} = \frac{16 K_c C_c q \cdot q_p}{3\pi \mu U D^2 d_p}$	For droplet and particles charged	(1-23)	[13]
$E_{Es,CD} = \left\{ \frac{15\pi}{8} \left(\frac{\varepsilon_p - 1}{\varepsilon_p + 2} \right) \frac{2C_c \left[q / (\pi D^2) \right]^2 d_p^2}{3\pi \mu_g U \varepsilon_0 D} \right\}^{0.4}$	Image force for Charged Droplet	(1-24)	[14]
$E_{Es,CP} = 2.89 \left\{ \frac{C_c q_p^2}{3\pi^2 \mu_g U \varepsilon_0 D^2 d_p} \right\}^{0.353}$	Image force for Charged Particles	(1-25)	[14]

THERMOPHORESIS, E_{Th}			
$E_{Th} = \frac{4a \left(2 + 0.6 \,\mathrm{Re}^{\frac{1}{2}} \,\mathrm{Pr}^{\frac{1}{3}} \right) (T - T_{as})}{UD}$		(1-26)	[13]
$a = \frac{2C_c (k_g + 5Kn \cdot k_p) k_g}{5P(1+6Kn)(2k_g + k_p + 10Kn \cdot k_g)}$		(1-27)	

DIFFUSIOPHORESIS, E_{Dph}			
$E_{Dph} = \frac{4b \left(2 + 0.6 \,\mathrm{Re}^{\frac{1}{2}} Sc_w^{\frac{1}{3}} \right) \left(\frac{P_w^{\circ}(T)}{T} - \frac{P_w^{\circ}(T_{as})}{T_{as}} RH \right)}{UD}$		(1-28)	[13]
$b = \frac{T D_w}{P} \sqrt{\frac{M_w}{M_g}}$		(1-29)	

Table 1-3 Models for collisional efficiency

In order to be defined, this capture model needs several information to be applied. The main phenomenon is the electrical interaction between particles and droplets. As reported in *Table 1-3* in *eq (1-23) (1-24) (1-25)*, particle and droplets charge need to be defined:

- *Particle charging*: particles are electrically charged through a corona system. According this phenomenon, a high ion concentration generated in a small area caused by a high electric field is responsible of the acquisition of charges by a particle. Particles, passing through this high electric field, are able to acquire electrical charges. A corona effect is the result of

electrical discharge that occurs between an electrode connected to high voltage and a grounded surface. The basic process of corona charging is reported in *Fig. 1-6*, which refers to a wire-tube geometry, with high potential wire (negative polarity) and grounded tube.

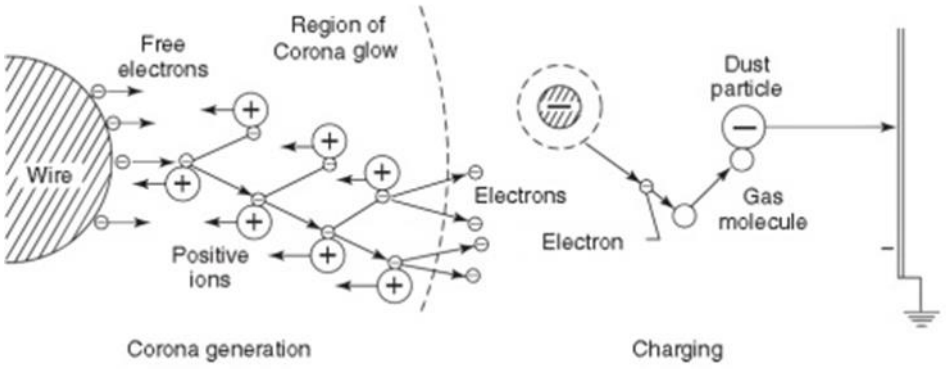

Figure 1-6 Basic process of corona discharging

The electric field is established between the electrode and the ground above a threshold voltage; for lower voltages the system works like an open electric circuit and no current flows between the electrode and the ground. When corona effect is present in the proximity of the electrode a characteristic bluish-green glowing appears. In this zone, the electrons accelerate and collide with neutral air molecules, ionizing them, or rather removing an electron producing another electron and a positively charged ion. Therefore, positive ions move to the electrode, while negative ions and electrons move to the grounded surface producing an ion flow.

As a consequence, particles which pass through a corona-ionized zone, acquire an electrical charge. According to the mentioned phenomenology, there are two different charging mechanisms: *diffusion charging* and *field charging*.

Diffusion charging entails random collisions between charged ions and/or electrons and particles, due to Brownian motion. Once particles have been charged, they tend to repel other ions and, therefore, the overall charging rate decreases. The charge acquired by a particle is a function of its diameter, d_p and its residence time in corona discharge.

Field charging occurs when the particles are subjected to an electrical field and, therefore, they are literally bombarded by ions. The presence of spherical particles induces a distortion of the electrical field lines and all the ions, which follow the field line intersecting the particles, collide with them and then transfer their charge to them. When particles start to be charged, they repel the incoming ions: the electrical field strength decreases as well as the

field lines converging on the particles. The particles reach a charge saturation value when no ions can collide with them, since no field lines converge on the particles anymore.

As for diffusion charging, the charge acquired by a particle due to field charging is a function of particle diameter and residence time.

When the intensity of the electric field, producing the corona discharge, starts to increase, it affects the electrons in the atomic orbitals and may cause atoms or molecules to polarize or liberate electrons. If the energy acquired by these electrons is higher than their ionic potential, they are able to leave the molecule and collide with other particles, causing the production of radicals.

- *Droplets charging*: For the case study, the induction is used for droplets charging. The electric charges on droplets are induced by polarization of the liquid jet caused by the electric field generated by an electrode. The droplet charges have opposite polarity to that of the electrode. This mechanism is used more than the others, in the WES concept systems, due to its constructive simplicity.

  The two relevant parameters to characterize charged drops are the ratio between actual charge and theoretical *Rayleigh charge*, q_d/q_R and the *charge to mass ratio (D-CMR).*

  The *Rayleigh limit* [15] is the highest electrical charge that can be present on a droplet of a given diameter, D, without making it unstable and eventually tearing it apart. It can be calculated using the *eq. (1-30*):

$$q_R = \sqrt{8\pi^2 \Gamma_w \varepsilon_0 D^3} \qquad (1\text{-}30)$$

  The *charge-to-mass ratio (or DCMR)* is the charge acquired by a droplet, divided by its mass.

  A description of induction charging of water is reported in the works of Jaworek and coworkers [16] and Di Natale and coworkers [17].

D'Addio et al. [8] proved that the particle capture model is able to describe particle abatement for a WES lab-scale system. For a well-controlled system, all the parameters are quite easy to acquire: particles charge is evaluable because of the simple geometry of particle charging unit (consisting of a wire and tube system) that is a wire and tube charging system; single droplets are sprayed and

electrically charged, therefore the *droplet charge to mass ratio* or *D-CMR* is gained and so the droplets distribution. The mathematical model is able to describe the particle capture efficiency for a well-controlled system, but when it is scaled up to the preindustrial scale, the evaluation of all the variables becomes quite difficult because the scavenging model is applied to a more complex phenomena and geometry. The problem is mainly related to both the fluid dynamic and corona charging phenomena related to particles, as well as all the interactions exiting between droplets and particles.

1.2 Aim of the work

This work contributes to the development of the technology of Wet Electrostatic Scrubbing (WES) at industrial scale by improving the current knowledge on corona charger unit design and designing, by building and setting up a pilot scale WES for specific industrial applications. This work was developed jointly by the Department of Chemical, Material and Industrial Production Engineering of the University of Naples Federico II" and the Ecology Division of the Boldrocchi s.r.l. .

As described in *Chapter 1*, the Wet Electrostatic Scrubber is an upgrade of a conventional wet scrubber: it was proved that the electric forces are the main responsible for particle capture, more than the other physical phenomena that might be present in the scrubber.

Therefore, the first topic covered by the study was the assessment of design criteria to scale up corona charger for particle charging. To understand the actual particle charge distribution of an ensemble of particles entering a corona device, several parameters have to be defined: particles residence time, local electric field and ion concentration, particle shape and composition. These parameters are generally considered on their mean value, but this approach is not adequate for predicting particle charges for a more complex system. For this reason, using the simulation program *Ansys Fluent* to gain some information concerning particle behavior in the reactor, two different particle charging models will be compared to experimental data.

To provide a reliable assessment of particle charge, we developed a particle capture model in a WES unit coupling the particle capture model presented in D'Addio et al [8] and Di Natale et al [7] with the results of a dedicated computational Fluid dynamic analysis performed using *Ansys Fluent*. The model was used to describe the experimental data obtained by our research group in a smaller WES pilot tested in several conditions during the EFP7 *DEECON* project. In particular, this model includes a dedicated assessment of droplets size and charge distribution, which can be achieved properly only by experimental data and the relevant fluid dynamic parameters as gas residence time

distribution, droplets spatial distribution and gas-droplets relative velocities, which are evaluated through the computational program *Ansys Fluent* (explained in *Chapter 3* in detail).

Averaged values of particle charges were determined using theoretical models and mean values of electric field, ion concentration and residence time in the pilot scale corona charger. This predictive model was applied to the case study and compared with the experimental data. In order to overcome the limited knowledge on particle charging, a reversed approach to data analysis was proposed. In this case, the data on particle capture in the WES were used to calculate the charge deposited on the particles and the achieved data were considered in terms of total aerosol current, applied voltage and particle size. A block diagram is shown in *Chapter 3* to better this new particle charging approach, since many variables should be defined and a complex *Matlab* routine was developed to reach this aim.

These information were used to define design and operating conditions for the pilot WES system (operating at gas flow rates ranging from 5500 to 10.000 Nm^3/h) build and operated at the Boldrocchi factory in Biassono (MB, Italy). The pilot scale system was operated in several conditions using reference Arizona test dust particles. The experimental data demonstrated that the WES units are able to achieve particle removal efficiencies higher than 90% in number, for particles from 150 to 800 nm, with results consistent with the design specifications. In order to better understand the aim of this work, in *Fig. (1-7)* a scheme is proposed.

Figure 1-7 Block diagram of the thesis work

Chapter 2. State of Art

In this chapter, all the charging model through corona discharge are reported. Starting with an explanation on the physic that regulates this phenomenon, several model to evaluate the particle charge are described in detail.

2.1 Discharge mechanisms

It is worth noticing that in different regimes, all discharges have in common that free ions and electrons in a gaseous atmosphere are involved. Different kind of discharges might be distinguished:

- Arcs: observed during thunder storms;
- Glow discharges: e.g. a gas at low pressure in a tube;
- Dark discharges: hard to be observed.

Discharges are distinguished not only by their luminescence but also by their Current-Voltage characteristics, the current density and breakdown voltage. These main characteristics depend on the geometry of the electrodes and the vessel, the gas used, the electrode material. Changing the discharge current, discharge regime is changed as well. *Fig. 2-1* shows the typical characteristic curve of a discharge tube.

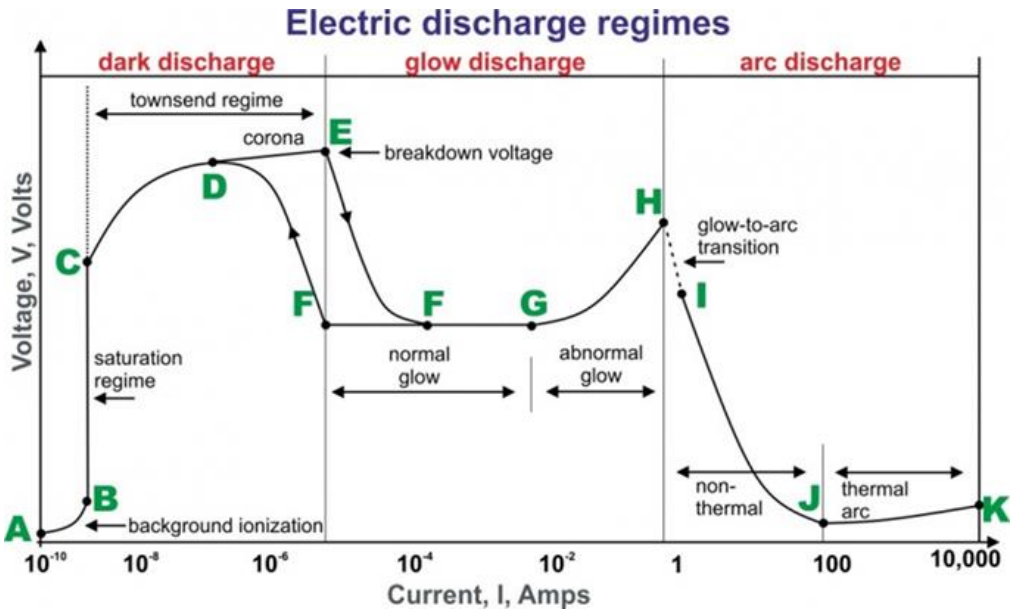

Figure 2-1 Voltage Current characteristic curve in different regime[18]

Dark Discharges

The regime between A and E is named dark discharge because, except for corona discharges and the breakdown itself, the discharge is not visible to the eye.

In the (A-B) area zone the background ionization occurs. The current increases with the voltage increasing, but very slowly. The electric field is not so high to cause an *electron avalanche*, that is a process in which free electrons are accelerated by an electric field and moved in a medium, they cause collisions with atoms.

In (B-C) area the potential is further increased and the current remains on a constant value, which means that it has reached its saturated value.

Beyond point C, the current rises exponentially. The electric field is high enough to let electrons initially present in the gas acquire sufficient energy. At this point, they are able to ionize a neutral atom and consequence, to create more free charged particles: the avalanche process has started and new electrons may have enough energy to ionize other neutral gas atoms. This region of exponentially increasing current is called the Townsend discharge [18] (C-E).

Corona discharge occurs in Townsend dark discharges in regions where the presence of a high electric field near sharp points, edges, or wires in gases causes an electrical breakdown. The electric field is the ruling parameter, rather than the potential between the electrodes. If the corona currents are enough (D-E), corona discharges can be visible to the eye, but for low currents, the corona is

dark. Corona discharges do not occupy the entire distance between the two electrodes, but are present only in the area where there is a high electrical field.

(D-F) is called the transition zone, also known as the pre-glow discharge area. It is a very instable area where the current grows following an exponential function while the voltage decreases until point E. The electrical breakdown occurs in the gas discharge tube and dazzling lightning can be observed.

When ions reach the cathode, they are able to generate secondary electrons (E), therefore the electrical breakdown occurs in Townsend regime. The breakdown voltage for a particular gas and electrode material depends on the product of the pressure and the distance between the electrodes, as expressed in Paschen's law [18].

Glow Discharge

The glow discharge regime is characterized by the typical luminous glow. Because of the plasma gas light, the electron energy is high enough to generate excited gas atoms by collisions. Furthermore, these excited gas atoms may be able to emit photons if they return to relax ground state.

In (F-G) region, the gas enters in the normal glow region where the voltage remains constant while the current grows over several orders of magnitude. In this regime, the plasma occupies the entire cathode surface (at point G) and when this happens, the only way the total current can grows is by increasing the current density through the cathode.

When the applied voltage increases with current causing an increasing in the average ion energy bombarding the cathode surface, the regime is called abnormal glow (G-H).

Due to the high current density, the cathode is hot enough to emit electrons thermionically, giving rise to an arc regime.

Arc Discharges

At point H, the cathode is so hot that is able to emit electrons thermionically. If sufficient current is supplied to the discharge, the regime is glow-to-arc transition, (H-I). In the arc regime (I-K) the voltage decreases while the current increases, until achieving point J. After that, the voltage increases again slowly with increasing current [18].

2.2 Corona discharge

To charge a particle in the WES pilot a corona discharge should be established. Townsend [18] was the first one to make experimental tests on gas discharge: it was noticed that when a gas is in a tube with a pressure under 200-300 mmHg, fixing the electric field at 25 kV/cm nothing happens if there is not an external source as ultraviolet radiation or an electron in the tube. In order to generate a discharge, you need initial electrons, called "seed electrons" coming from the cathode (the electrode connected to the negative voltage). After this generation, electrons migrate to the anode and impact with gas molecules. This phenomenon is responsible of three processes:

- α-process: while electrons are moving to the anode (the positive electrode) they impact with gas molecules and if the kinetic energy of the collision is higher than the ionization one, the atom will lose its external electron. In this way, from the first electron generates two and these ones will turn into four because of the collision and so on.
  Considering α coefficient as the number of electrons produced due to the strike per cm and if *d* is the distance between electrodes, taking into account a layer of thickness *dx*, a number n_{ex} of electrons is produced as shown in *eq. (2-1)* and sketched in *Fig. 2-2*:

$$dn_{ex} = n_{ex}\alpha\, dx \qquad (2\text{-}1)$$

  Setting the boundary condition $x=0$ and $n_{ex}=n_{e0}$ where n_{e0} is the number of electrons at the cathode, it is possible to obtain the eq (*2-2*):

$$n_{ex} = n_{e0}e^{\alpha x} \qquad (2\text{-}2)$$

  When the avalanche of electrons arrives to the anode, so when $x= d$, the *eq.* (*2-3*) is obtained:

$$n_{ed} = n_{e0}e^{\alpha d} \qquad (2\text{-}3)$$

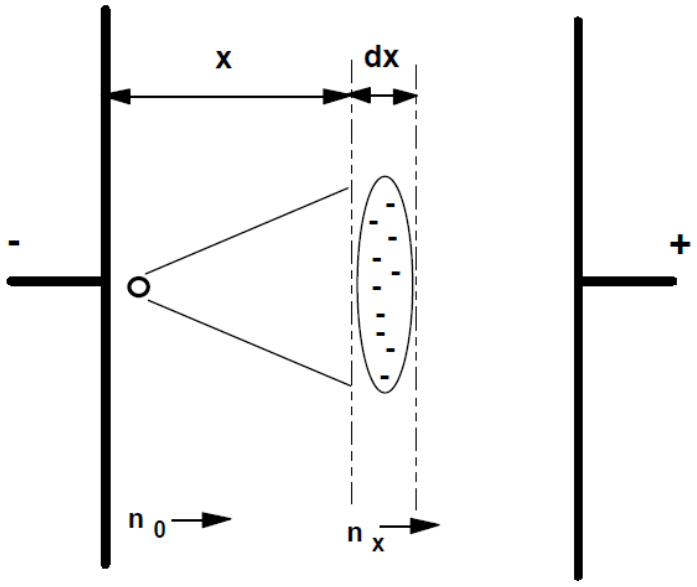

Figure 2-2 Electron avalanche [18]

Since there is a movement of electrons through two electrodes, a current (*eq. 2-4*) is produced:

$$i_{ea} = i_{e0} e^{\alpha d} \qquad (2\text{-}4)$$

Where i_{ea} is the electric current carried by electrons that collide with the anode and i_{e0} is the current corresponding to n_{eo} charge concentration.

According to Townsend theory [18], α (known as the *first ionization coefficient*) depends on applied electric field and on gas pressure, as reported in *eq. (2-5):*

$$\frac{\alpha}{P} = f_1\left(\frac{E}{P}\right) \qquad (2\text{-}5)$$

α depends on the energy during the free path related to electric field. Under the assumption that $\overline{\lambda_e}$ is the electron mean free path, the probability that an electron is able to ionize gas particles during its path depends exponentially to the applied voltage on the electrodes and on electric field. Therefore, it is possible to write a dependence between the first Townsend coefficient and the electric parameters as reported in *eq. (2-6)*:

$$\alpha = \frac{1}{\overline{\lambda_e}} exp\left(-\frac{V}{E\,\overline{\lambda_e}}\right) \qquad (2\text{-}6)$$

Since $\overline{\lambda_e}$ is inversely proportional to gas density, i.e. inversely proportional to the gas pressure, the *(1-5)* is explained.

- β-process: every time that there is a formation of a new electron, in parallel the generation of a positive ion occurs. The ion will migrate toward the cathode. The *second ionization* β represents the number of ionizing collisions generated by positive ions. Since the positive ions have a kinetic energy four order of magnitude lower than that of the electrons, $\beta \ll \alpha$;
- γ-process: due to the α-process, $n_{e0}(e^{\alpha d} - 1)$ positive ions are produced, strike cathode surface and generate a new avalanche of electrons. The *third ionization coefficient* γ represents the electrode surface ionization due to the impact of positive ions on the cathode. The amount of
  this new avalanche is given by $\gamma n_{e0}(e^{\alpha d} - 1)$ that is called secondary avalanche (*eq. 2-7*).

$$n_{ed} = n_{e0} exp(\alpha d) + \gamma n_{ed}\, exp(\alpha d) \qquad (2\text{-}7)$$

So a new expression of electron number is given (*eq. 2-8*):

$$n_{ed} = \frac{n_{e0} exp(\alpha d)}{1 - \gamma\,(exp(\alpha d) - 1)} \qquad (2\text{-}8)$$

And so a new current (*eq. 2-9*):

$$i_{ed} = \frac{i_{e0} e^{\alpha d}}{1 - \gamma\,(exp(\alpha d) - 1)} \qquad (2\text{-}9)$$

Regarding at *eq. (2-9)*, there is a critical condition: for $(exp(\alpha d) - 1) = 1$. When there is no an applied voltage, the current ends and it means that electrons are generated only by α-process. But if γ-process occurs, so there is the formation of secondary electrons and in particular if $\gamma = 1$, a discharge will occur even if there is not any external source applied on

the device. This condition is known as self-sustaining discharge. Townsend [18] proved that there is a relation between α and γ coefficients, as reported in *eq. (2-10).*

$$\alpha d = ln(1/\gamma) \qquad (2\text{-}10)$$

γ coefficient depends on the electrode matter, gas type and on the number of ions (*eq. 2-11*), regarding at *eq (2-6)* and replacing α in *eq. (2-10)*, it is possible to obtain a dependence of γ on $\overline{\lambda_e}$, that means on gas pressure [18]:

$$\gamma = f_2(Pd) \qquad (2\text{-}11)$$

Where *P* is the pressure and *d* is the electrodes distance.
Starting from Townsend experience, Paschen [19] found out a correlation between the voltage breakdown (V_b) and the product *Pd (fig. 2-3)*, that depends on gas nature, electrode matter, pressure *(eq. 2-12).*

$$V_b = f(Pd) \qquad (2\text{-}12)$$

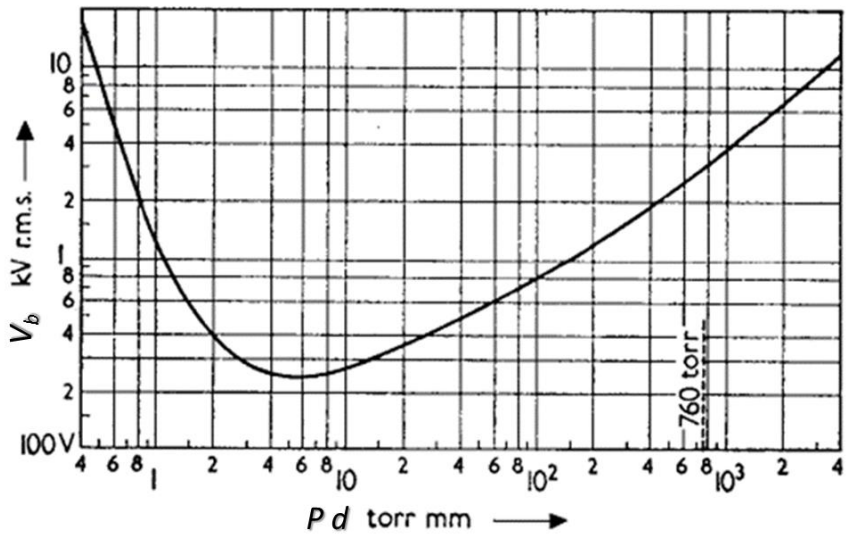

Figure 2-3 Paschen curve for air

There are two scenarios:

- $Pd<(Pd)_{min}$: the number of collisions is not enough to let the breakdown happen because the pressure is too low comparing to the minimum of the function, or the electrode distance is too small to allow electrons reaching high enough kinetic energy;
- $Pd>(Pd)_{min}$: the energy acquired by electrons is not enough since the free path is lower and this happens because the pressure is too high comparing to the minimum (or the electrode distance is too high)

When the product *Pd* is over 200 cm mmHg, Meek [20] proved that Townsend theory is not able to explain discharge mechanism because it does not take into account:

1) discharge timing formation: the appearance of sparks at high pressure (considering a suitable value of d) cannot be explained just by Townsend α coefficient.
1) cathode matter: at atmospheric pressure it was demonstrated that there is no link between electrode material and sparking voltage;
2) spark shape: sparks formation takes place in tight channels and not because of charges waves;

According to Meek [20], during the formation of an avalanche the effect of spatial charge concentration should be taken into account. During their path, negative ions modify the electric field as shown in *Fig. (2-4)*.

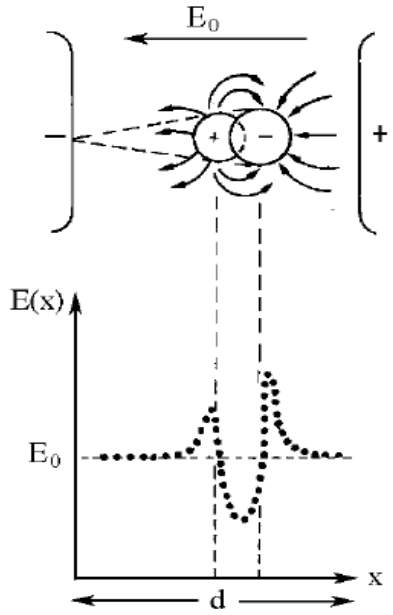

Figure 2-4 Electric field during electron avalanche

Therefore, it is clear that the electric field could not be considered uniform. There are two peaks, at the beginning and at the ending of the avalanche with a strong decreasing in the area behind the electronic cloud. Loeb [21] proved that where positive and negative ions exist the discharge is also caused by recombination phenomena with the release of photons as consequence.

Photons have a high energetic content and they are accelerated by the electric field, giving birth to secondary avalanches; they are also able to neutralize part of the primary avalanche and start up a partial ionized area.

At this point, positive ions that are behind the second avalanche form a spatial charge closer to the cathode, which will move with a higher velocity: their flow will not depend on ion movement but on formation of secondary avalanches.

Replying this phenomenon, the result will be a positive charge moving from the anode to the cathode, leaving behind a stream partially ionized *(Fig. 2-5)*.

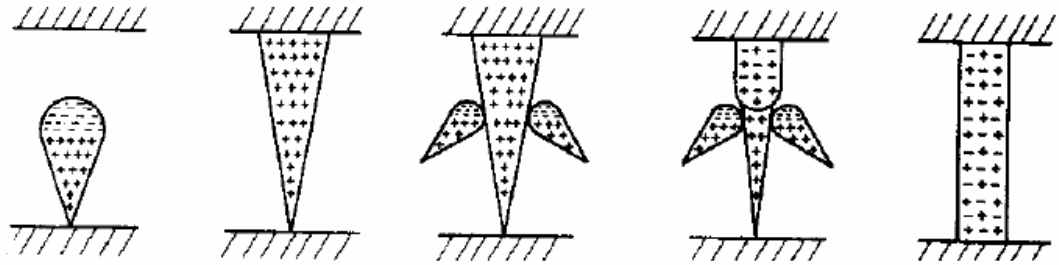

Figure 2-5 Spark discharge formation

The stream is not a linear filament, since the spatial charges both negative and positive are radial so the consequence is the formation of branches from the anode to the cathode.

This result explains how the streamer formation is linked to avalanche dimension near the anode.

According to Meek [20] e new relationship between α and electric field is proposed *(eq. 2-13)*:

$$\alpha d + ln\frac{\alpha}{P} = 14.46 + ln\frac{E}{P} + \frac{1}{2}ln\frac{d}{P} \qquad (2\text{-}13)$$

Corona discharge could be generated where there is a strong electric field applied on a sharp electrode with a small geometry like needles or wires. It was proved [20] that for lower values of *Pd* (*Pd*<200 cm mmHg) Townsend theory is able to explain the discharge phenomena, while for higher values, the effect of photons on avalanche formation is more relevant, as shown in *(Fig. 2-6)*.

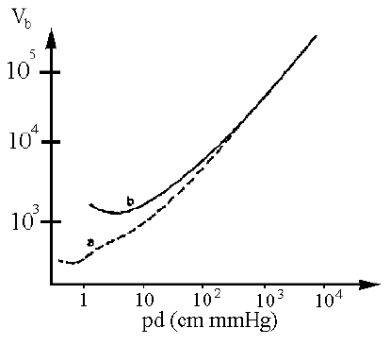

Figure 2-6 Experimental (a) and theoretical (b) curves to show the relationship between breakdown voltage and Pd [20].

In order to establish a corona discharge, a sharp electrode is necessary. Corona is generated by strong electric fields associated with small diameter wires, needles or sharp edges on an electrode (*Fig. 2-7*), even though these discharges needs a low power electrical discharge.

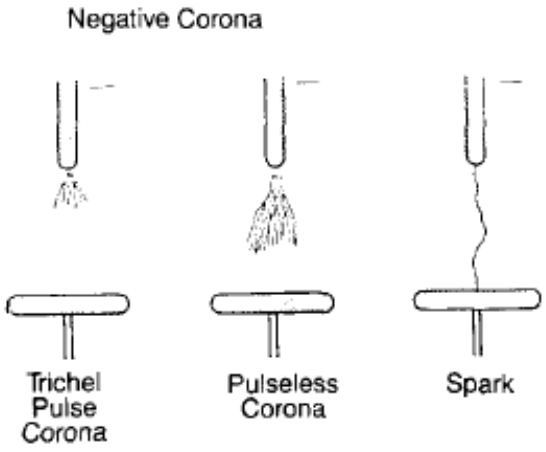

Figure 2-7 Schematic of type of corona discharges [22]

Apart from particle charging, corona discharge is a widely used mechanism, e.g. for ESP systems in order to electrically charge and then remove particle pollutants, ozone production, chemical ionization at atmospheric pressure, several models are proposed in literature to implement and solve corona mechanism. Lapple [23] was the first one to propose models to design corona charging units. Several authors (: Lawless [24], Chang [22], Porteiro [25] and Zhuang [26]) studied this model in a modern key.

The gas fluid dynamic and the Maxwell-Boltzmann equations (from *eq. (2-14) to (2-33)*). In particular:

$$\nabla \cdot \bar{E} = \frac{\rho_c}{\varepsilon_0} \quad (2\text{-}14)$$

$$\nabla \cdot \bar{B} = 0 \quad (2\text{-}15)$$

$$\nabla \times \bar{E} = 0 \quad (2\text{-}16)$$

$$\nabla \times \bar{B} = \mu_0 \bar{J} \quad (2\text{-}17)$$

By definition of electric potential,

$$\bar{E} = -\nabla V \quad (2\text{-}18)$$

And *eq. (2-18)* becomes:

$$\nabla^2 V = \frac{\rho_c}{\varepsilon_0} \quad (2\text{-}19)$$

Current continuity is implicit in e*q. (2-17)* and can be obtained by applying the divergence operator to both sides of the equation, resulting e*q. (2-20)*

$$\nabla \cdot \bar{J} = 0 \quad (2\text{-}20)$$

The electric current density is the sum of four terms (*eq. (2-21)*):

$$\bar{J} = \rho_{ion} b_{ion} \bar{E} + \rho_{ion} \bar{v} + \rho_p \bar{v}_{cell} - D_e \nabla \rho_{ion} \quad (2\text{-}21)$$

The first member represents ion movement due to the electric field, the second one due to the gas. The third charged particles and the last because of the density gradients.
Near the electrode, in a very small region when the corona discharge occurs, a high concentration of ions is generated and this cause the saturation of the electric field [25]. The value of the electric field is evaluated through Peek's law for negative corona (eq. *(2-22)*).

$$E_{Peek} = \left[3 \cdot 10^6 \delta + 9 \cdot 10^4 \sqrt{\frac{d}{r_w}}\right] \cdot f \cdot f_h \qquad (2\text{-}22)$$

$$f_h = (1.27 \cdot 10^{-5}) h_a^2 - (3.32 \cdot 10^{-3}) h_a + 1 \qquad (2\text{-}23)$$

Where f_h is the humidity coefficient that becomes relevant in streamer formation because water vapor acts like an electronegative gas, decreasing the possibility of arcs generation.
Electro-magnetic field equations and the same definition of *J* implies correlation with fluid dynamic:

$$\frac{\partial \rho}{\partial t} + \nabla \cdot (\rho \bar{v}) = 0 \qquad (2\text{-}24)$$

$$\frac{\partial}{\partial t}(\rho \bar{v}) + \nabla \cdot (\rho \bar{v} \bar{v}) = -\nabla P + \nabla \cdot (\bar{\bar{\tau}}) + \bar{F} \qquad (2\text{-}25)$$

$$\frac{\partial}{\partial t}(\rho h) + \nabla \cdot (\rho \bar{v} h) = \frac{\partial P}{\partial t} + \bar{\bar{\tau}}(\nabla \cdot (\bar{v})) + S_h \qquad (2\text{-}26)$$

When particles and gas molecules are ionized, you should add to the system another *eq. (2-27)*:

$$\bar{F} = \rho_{ion} \bar{E} \qquad (2\text{-}27)$$

For a negative corona, when the electric field *E* is high enough and the mean free path is large (for high temperature systems), larger particles (d_p > 2 μm) are charged by *field charging* mechanism. The amount of charges, under the hypothesis of spherical particle, is given by Pautheniers' theory [27] (*eq. (2-28)*) This theory found its validity for coarse particles and for $Kn \ll 1$ (Knudsen number), that is the continuum field, where the fluid dynamic can be described by Navier-Stokes equations.

$$q_{field} = \frac{q_s\left(\frac{t_r}{\tau}\right)}{1+\frac{t_r}{\tau}} \qquad (2\text{-}28)$$

Where q_s is the saturation charge *(eq. 2-29)*:

$$q_s = 12\pi\varepsilon_0 \left(\frac{d_p}{2}\right)^2 E \frac{\varepsilon_r}{\varepsilon_r+2} \qquad (2\text{-}29)$$

And τ is the charging time *(eq. 2-30)* and constant for particles:

$$\tau = \frac{4\varepsilon_0}{N_i e Z_i} \qquad (2\text{-}30)$$

Where N_i is the ion concentration that depends on the electric field E through which the particles travel and q_s represents the saturation limit called Pauthenier limit [27]. For field charging mechanism, there is a quadratic dependence on particle diameter d_p.

Particles with $d_p < 0.2$ µm are generally mainly charged by *diffusion charging*, called also thermal *diffusion mechanism*. This phenomenon was largely studied by Fuchs [28], who introduced *the limiting sphere theory*. in the absence of an external electric field, the diffusion of gas ions *(eq. 2-31)* toward a spherical particle is:

$$\frac{\partial n}{\partial t} = D \frac{\partial^2 n}{\partial^2 \rho} + \frac{2D}{\rho} + B \frac{\partial}{\partial \rho}[\rho^2 n F(\rho)] \qquad (2\text{-}31)$$

Where

ρ is the distance from the center of the particle;

n is the concentration of the ions under consideration

D diffusivity coefficient

B is the mobility referred to a force of 1 dyne

F is the electrostatic force acting on the ion

Under the hypothesis of a steady flux of ions toward the particle, the current *(eq. 2-32)* generated by the flux of ions is:

$$I = 4\pi\rho^2 \left(D \frac{\partial n}{\partial \rho} - BFn\right) \qquad (2\text{-}32)$$

Putting $n = n_0$ and for $\rho=\infty$, where n_0 is the initial ion concentration, *eq. (2-33)* is the integral of *eq. (2-32)*:

$$n(\rho) = exp\left[-\frac{B}{D}\varphi(\rho)\right]\left\{n_0 + \frac{I}{4\pi D}\int_{\infty}^{\rho}\frac{1}{\rho^2}exp\left[\frac{B}{D}\varphi(\rho)\right]d\rho\right\} \qquad (2\text{-}33)$$

Where φ is the potential energy of the ion, expressed in *eq. (2-34)*:

$$\varphi(\rho) = \int_{\infty}^{\rho} F(\rho)\, d\rho \qquad (2\text{-}34)$$

Neglecting the ion concentration jump at the surface of the particle, for $n=0$ and for $\rho = r_p$, with r_p as particle radius, it is possible to consider a sphere that surrounds the particle having a diameter δ *(eq. 2-35).*

$$\frac{\delta}{r_p} = \frac{r_p^2}{\lambda^2}\left[\frac{\left(1+\frac{\lambda}{r_p}\right)^5}{5} - \frac{\left(1+\frac{\lambda^2}{{r_p}^2}\right)\left(1+\frac{\lambda}{r_p}\right)^3}{3} + \frac{2}{15}\left(1+\frac{\lambda^2}{{r_p}^2}\right)^{5/2}\right] \qquad (2\text{-}35)$$

Where λ is the mean free path of the gaseous ions.

Substituting $\rho=\delta$ in *eq. (2-32)* and *(2-33)*, it is possible to obtain the ion concentration and current in dependence of limiting sphere.

Inside this sphere particle's behavior is similar to that one of a molecule in vacuum. Outside the sphere, ion Brownian motion could be described by the macroscopic theory of diffusion. On particle surface, kinetic gas and diffusion theories are equivalent.

In case of the absence of any electrical forces, the collision probability ψ (*eq. (2-36)*) reduces to:

$$\psi = r_p^2/\delta^2 \qquad (2\text{-}36)$$

While for charged particles, the collision probability is given by the collision parameter b (*eq. (2-37)*):

$$b^2 = r^2\left[1 + \frac{2}{3kT}\left(\varphi(\delta) - \varphi(\rho_m)\right)\right] \qquad (2\text{-}37)$$

Where ρ_m is the minimal distance between the particle center and the trajectory of the ion moving on the limiting sphere with a mean thermal kinetic energy. The minimum collision parameter (*eq. (2-38)*) is given when $r_p = b_m$, so the associated collision probability is:

$$\psi = b_m^2/\delta^2 \qquad (2\text{-}38)$$

Fuchs stated that the probability is one if the only attractive encounters are considered.
These studies were carried out also by Hopple et al. [29], proving that the collision probability is not equal to the unity. Furthermore, Biskos [29] shows that Fuchs' theory is valid when there is a low concentration of ion. For a higher concentration of ion, Boisdron and Brock [29] 's theory "*birth-to-death* " (*eq. (2-39)*) gives the solution to an infinite set of differential equations:

$$\frac{dN_{P,0}}{dt} = -\beta_0 N_{P,0} N_i$$

$$\frac{dN_{P,1}}{dt} = \beta_0 N_{P,0} N_i - \beta_1 N_{P,1} N_1 \qquad (2\text{-}39)$$

$$\vdots$$

$$\frac{dN_{P,n}}{dt} = \beta_{n-1} N_{P,n-1} N_i - \beta_n N_{P,n} N_i$$

Where $N_{p,n}$ is the number concentration of particles with n elementary charges, N_i is the ion concentration, $\beta_n = J/N_i$ is the combination coefficient of ions with particles carrying *n* elementary charges and *J* is the ionic flux to the particle. Solving this system, the evolution of the charge distribution on monodisperse particles is acquired. In spite of field charging, diffusion mechanism prevails for $Kn \gg 1$ and for $Kn \approx 1$, when the molecular regime is able described the fluid dynamics. The prediction of a charge distribution is hard to acquire because it is hard to predict ions produced by corona discharges. Boltzmann [30] proposed a charge distribution having a Gaussian shape. Even though, this law is valid under equilibrium and not on stationary state, Biskos [29] and White [31] proved its validity, comparing this theoretical approach with experimental tests.
Furthermore, to account particle trajectories the following force balance is required (from eq. (*2-40*) to *(2-45)).*

$$\bar{F}_e + \bar{F}_d = m\frac{dv}{dt} \quad (2\text{-}40)$$

$$\bar{F}_e = q\bar{E} \quad (2\text{-}41)$$

$$\bar{F}_d = \frac{3\pi\mu D_p}{C_c}(\bar{v} - \overline{u_p}) \quad (2\text{-}42)$$

$$C_c = 1 + Kn\left[a + b\ exp\left(\frac{-c}{Kn}\right)\right] \quad (2\text{-}43)$$

$$Kn = \frac{2\lambda}{D_p} \quad (2\text{-}44)$$

$$\lambda = \frac{\mu}{P}\sqrt{\frac{\pi R_g T}{2}} \quad (2\text{-}45)$$

It is clear that the evaluation of the particle charge is not so easy because of the complexity of the system presented. Furthermore, the main variables as electric field, ionic concentration, charging time vary punctually in space where the corona discharge is established, that makes their estimation hard to acquire. For this reason, some approximations are used to solve this problem:

- Uniformity of the Electric Field
- Mean residence time
- Mean value of ionic concentration

Under these hypotheses, once fixed the particle diameter, a mean value of the electric charge is considered both for field charging and diffusion charging.
For coarse particles, the expression is given by Pauthenier (*eq. (2-34)*) and for fine particles the *eq. (2-46)* proposed by Flagan [32] is used:

$$q_{diff} = \frac{d_p k_B T}{2k_e e}\ ln\left[1 + \frac{\pi K_e d_p c_i e^2 N_i t_r}{2k_B T}\right] \quad (2\text{-}46)$$

Therefore, the charge acquired by a particle diameter is given by the sum of field and diffusion charging terms (*eq. (2-47)*):

$$q(d_p) = q_{diff}(d_p) + q_{field}(d_p) \qquad (2\text{-}47)$$

This approximation was used by Porteiro [25] and gives back as result a good match between experimental and theoretical data.

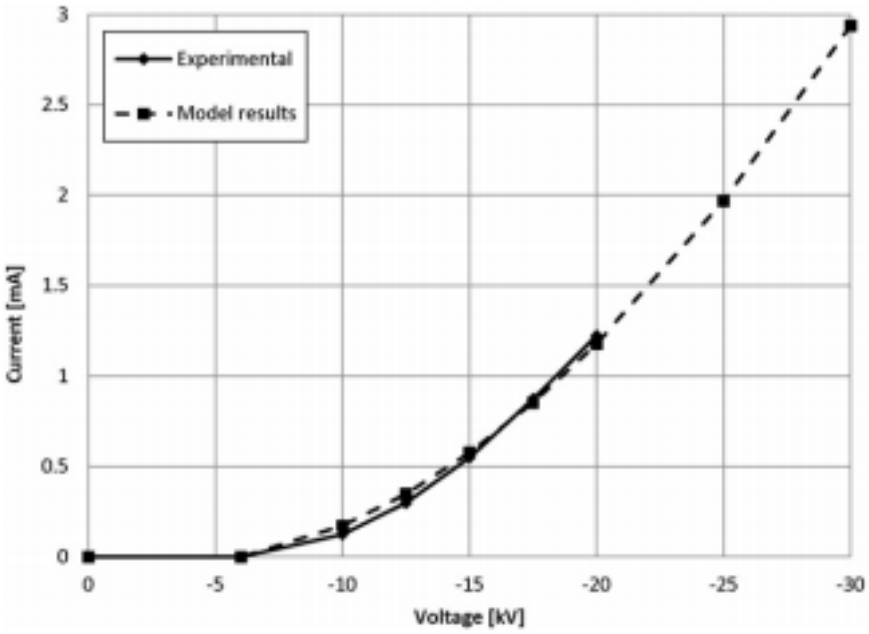

Figure 2-8 Comparison between the experimental and the model results V-I characteristic curves (using eq. (2-34) (2-46) and (2-47) for particle charging). [25]

Porteiro's work demonstrated that a suitable estimation of mean charge allows a good description of the V-I characteristic curve.

Chapter 3. Particle capture model

D'Addio et al. [8] proved that scavenging model described in *Chapter 1.2* is able to describe particle capture for a lab-scale system if the particle charge is known.

In this work we reversed the paradigm of D'Addio et al. [8] studies: starting from available WES experiments on particle capture and from the experimental determination of droplet charge and size distribution and of corona current, we reversed the model equations to gain information on the particle charge, either by testing existing models or by defining a new experimental model.

The case study is a WES pilot (*DEECON* prototype) and the results of the experimental tests are used to compare the particle capture model.

This is described by two approaches.

- Aerosol current approach: in order to evaluate the particle charge, the charging model used by Porteiro [7] and described in *Chapter 2.2* is used. To have a good match between experiments and theory, a comparison between theoretical current and experimental one was realized (*Fig. 3-1*).

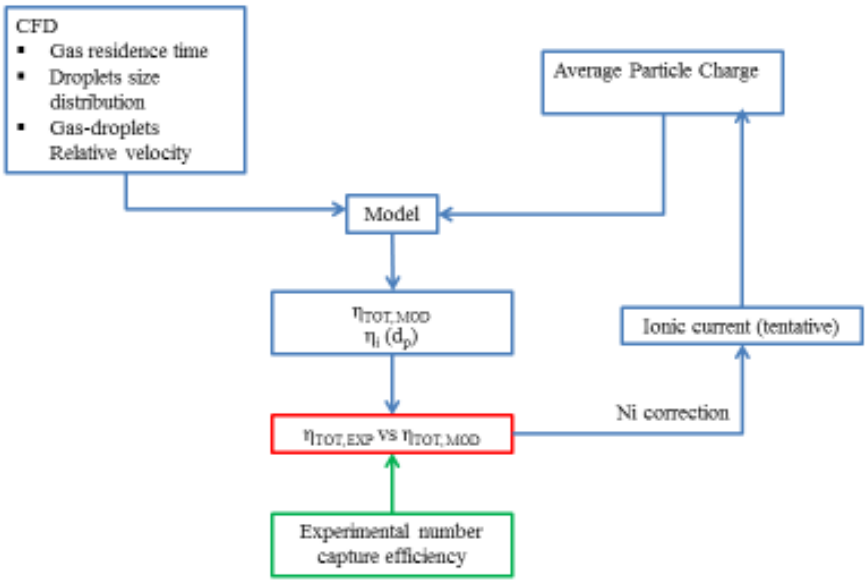

Figure 3-1 Scheme of Aerosol current approach

- Particle charge distribution based approach: once fixed the particle diameter, a charge distribution is used to estimate particle charge (*Fig. 3-2*).

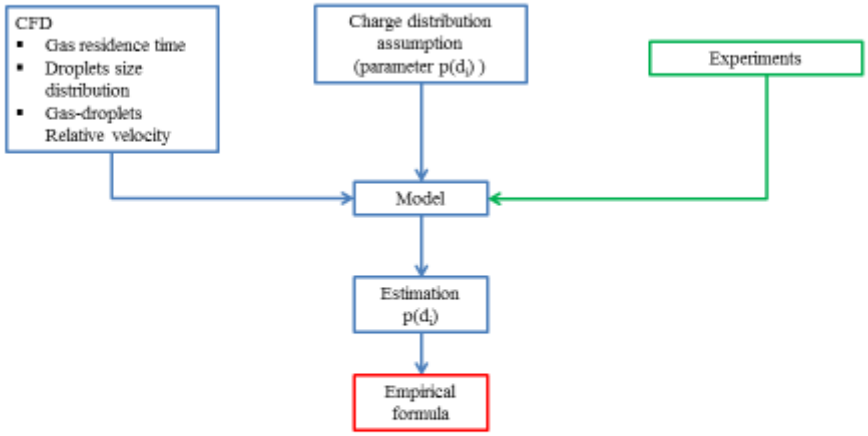

Figure 3-2 Scheme of Particle charge distribution approach

The particle capture efficiencies coming from these two particle-charging models will be compared to experimental data of a case-study WES system that will be described in this Chapter. As reported in *Chapter 1.3*, a fluid dynamic study is needed through the software *Ansys Fluent*. In post-processing droplets distribution, their velocity and gas residence time in the reactor are acquired. Using *Matlab*, the capture model is applied comparing the two charging models.

3.1 Experimental setup: case study

The WES column used in the case study analyzed there in is shown in *Fig. 3-3* and was the first prototype of Wet Electrostatic Scrubber tested by University of Naples during the *DEECON* project.

Figure 3-3 DEECON WES Pilot

The system consisted in an inlet tube, head of the column, column, bottom of the column, particle charging unit and electrified sprays.

The wet electrostatic scrubber was made from a stainless steel cylinder of inner diameter of 40 cm and 3.5 m high. It was equipped with a single-fluid pressure-swirl full-cone nozzle for generating a water spray electrified by induction (ES) to positive polarity, and with a particle charging unit (PCU) that used a corona source to ionize the gas for charging the particles with negative charge. The particle-laden gas stream and the cleaning-water spray flowed co-currently downward along the scrubber. A demister, with 50mm cutoff diameter, was placed in the pipeline at the exit of the scrubber to remove the droplets entrapped in the outflowing gas. The scrubber system was equipped with appropriate instrumentation to allow online measurement and control of gas and water flow rates, pressure drops, gas temperature and humidity, and charging potentials at the ES and PCU

electrodes. Particles are negatively charged in a corona charging unit PCU at different potentials (V_{PCU} = 15, 13, 11, 9, 7, 5 kV). Discharge current at PCU and current to the induction electrode in ES were also measured in order to estimate the power consumed by the electrostatic processes. The charged water spray was generated by a full-cone nozzle (models 460-484, Lechler) with a 45° of spray cone angle, equipped with a toroidal induction electrode connected to high voltage supply, operating at different voltages (V_{ES} = 13, 15, 17.5, 20 kV). The water flow rate was kept constant at 195 kg/h. The cumulative size distribution of electrosprayed droplets (*Fig. 3-4*) was measured with a Kamika AWK D infrared light scattering analyzer. The droplet size distribution was found to follow the Rosin–Rammler model [7]:

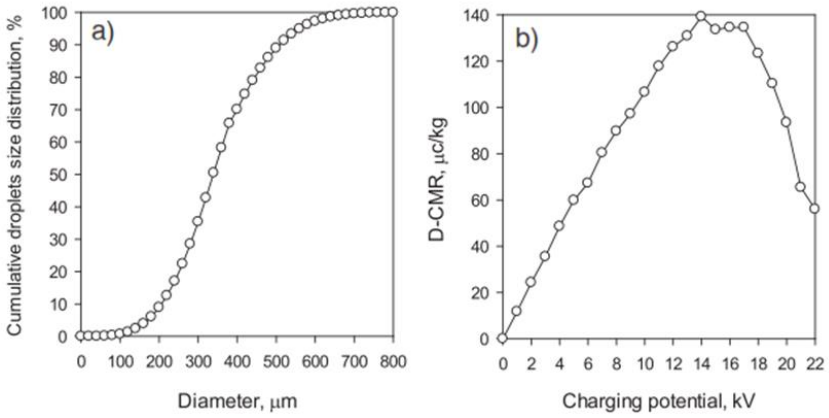

Figure 3-4 a) droplets diameters; b) D-CMR for each potential applied on the toroidal electrode[7]

In *Fig. 3-5* particle capture efficiency is reported, obtained at one of the experimental conditions: for V_{ES} = - 15 kV, V_{PCU} =- 15 kV and Liquid on Gas ratio of 0.88 kg/kg.

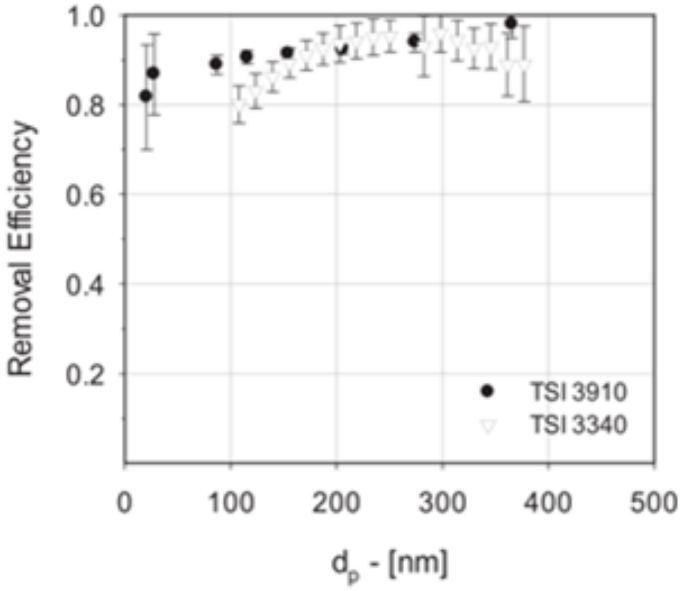

Figure 3-5 Capture efficiency as a function of particle size determined with TSI 3910 (black circles) and TSI 3340 (white triangles). V_{ES} = - 15 kV, V_{PCU} = - 15 kV, L/G= 0.88 kg/kg.

3.2 Fluid dynamic study

As described in *Chapter 3.1*, through fluid dynamic it is possible to acquire some variables hard to define but necessary for numerical particle capture estimation: water droplets, gas residence time and gas-droplets relative velocity. Through the simulation program *Ansys Fluent* it is possible not only to achieve all these variables, but also observing their evolution along the column.

3.2.1 Geometry and Mesh

The *DEECON* WES unit was drawn using *Solidworks*® (*Fig. 3-6)*, stretching input and output channels to allow a fully developed flow.

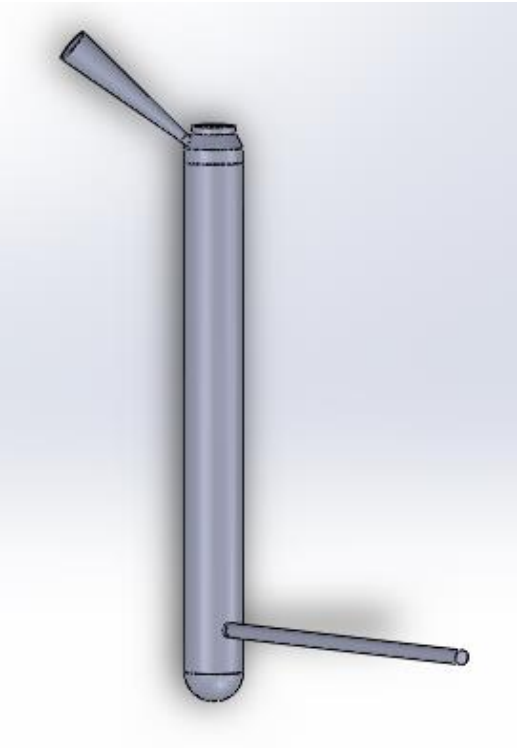

Figure 3-6 Deecon WES unit designed using Solidworks

Once drawn the geometry, three different meshes were created and compared. The main parameters to evaluate a good mesh are the *element quality* that represents the deviation of each cell from tetrahedric cell (that should be lower than 0.25) and the aspect ratio that regards the size uniformity of cells (that should be lower than 11). These parameters allow establishing the good quality of a mesh. *Table 3-1* shows the number of elements, the element quality and the aspect ratio of the worst element of each mesh. In order to choose the most suitable mesh, a sensitivity study was performed comparing the three meshes taking into account the net force on the bottom and the value of velocity integral on a plane.

After a comparison in a reference test (for G= 125 m^3/h), mesh 1 was chosen for the examination because it is excellent in terms of computational costs and accuracy of the elements in it drawn: regarding at *Table 3-1* it clear that for mesh 1 the tolerance between the smallest and the bigger mesh element is lower than 10%.

Mesh name	*Number of elements*	*Element quality*	*Aspect ratio*	*Pressure at the bottom*		*Velocity integral*	
	-	-	-	Smallest element	*Biggest element*	Smallest element	*Biggest element*
Mesh 1	1949886	0.21	9.109	0.26	0.2	0.81	0.88
Mesh 2	3002457	0.22	9.8	0.26	0.23	0.82	0.87
Mesh 3	345941	0.21	10.3	0.3	0.21	0.8	0.88

Table 3-1 Characteristic of the three meshes

The net force component along the z direction is computed by summing the product of pressure and viscous forces on bottom face with the specified force vector.
The terms represent pressure and viscous force components in the direction of the vector z, reported in *eq. (3-1)*:

$$F_z = zF_p + zF_v \qquad (3\text{-}1)$$

And the pressure on the bottom is calculated in the (*eq. (3-2)*):

$$P_b = \frac{F_z}{A_b} \qquad (3\text{-}2)$$

The velocity integral on a surface is computed by summing the product of the facet area and the velocity field variable face value, *eq. (3-3)*:

$$Q_{surf} = \sum |v| \, A_f \qquad (3\text{-}3)$$

$|v|$ is the velocity absolute value *(eq. (3-4))*:

$$|v| = \sqrt[2]{v_x^2 + v_y^2 + v_z^2} \qquad (3\text{-}4)$$

And the velocity on selected plane, is calculated in the *eq. (3-5*):

$$v_{surf} = \frac{Q_{surf}}{\rho_g Area_{column}} \qquad (3\text{-}5)$$

It is worth noticing that the chosen mesh presents a higher number of elements at the top of the scrubber where the fluid dynamic should present a recirculation of particles and drops (*Fig. 3-7*).

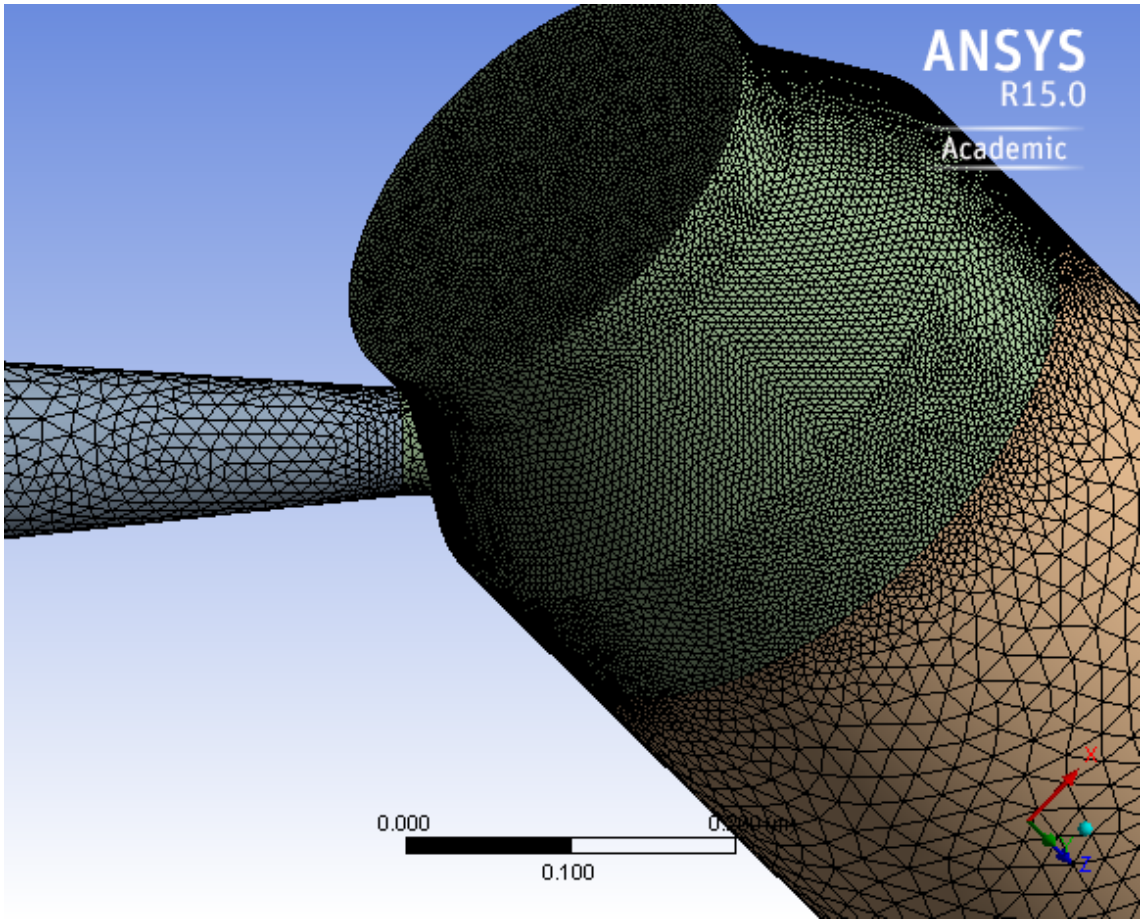

Figure 3-7 Mesh of a particular of the WES column

3.2.2 Gas turbulence model

To define the regime, a previous analytic evaluation was realized. In particular, *Reynolds number* (*eq. (3-6)*) was estimated for two different diameters: the inlet diameter and the chamber one, obtaining values respectively: 2.12 10^5 and 6.92 10^4, indicating that the fluid dynamic field is surely turbulent (>2100)

$$Re = \frac{\rho \, v \, D_c}{\mu} \qquad (3\text{-}6)$$

The first step was the valuation of Mach number defined as the characteristics speed of the fluid and the speed of sound ratio, to verify the hypothesis of incompressible gas. It was chosen the velocity in the inlet tube, because this is the highest value in the experiments. The speed of sound is u_s = 331.45 [m/s] and the U_{max} = 5.1 [m/s], $Ma=u_s/u_{max}=0.0153$, therefore it is possible the hypothesis to consider the fluid of incompressible since transition to compressible fluid approximation took place at Ma > 0.3.

The CFD code assumed:

1) Hypothesis of ideal gas (P= 1 atm);
2) Incompressible gas (Ma< 0.3);
3) Density constancy;
4) No heat generation;
5) Negligible viscous dissipation. Calculating the Brinkman number, the ratio between heat produced by viscous dissipation and heat transported by molecular conduction. i.e., the ratio of viscous heat generation to external heating: $\mathrm{Br} = \frac{\eta * U_\infty^2}{k * \Delta T} \sim 10^{-4} \ll 1$, where T is temperature, U_∞ is the flow velocity, η is the dynamic viscosity and k the thermal conductivity;
6) No reaction in the system;
7) Validity of Boussinesq's relation, to link Reynolds' tensor to mean velocity
8) Steady state conditions

One of the most effective viscosity models for the simulations of the turbulent flow is the Harlow-Nakayama *k-ε* model. Robustness, economy, and reasonable accuracy for a wide range of turbulent flows explain its popularity in industrial flow and heat transfer simulations. It is a semi-empirical model based on model transport equations for the turbulence kinetic energy (*k*) and its dissipation rate (*ε*), and the derivation of the model equations relies on phenomenological considerations and empiricism.

As the strengths and weaknesses points of the standard *k-ε* model have become known, improvements have been made to the model to improve its performance (from *eq. (3-7) to (3-11)*).

$$\nabla \cdot \boldsymbol{v} = 0 \qquad (3\text{-}7)$$

$$\boldsymbol{v} \cdot \nabla \boldsymbol{v} = -\frac{1}{\rho}\nabla P + \frac{\eta}{\rho}\nabla^2 \boldsymbol{v} + \nabla \cdot \left(2\eta_t \bar{\boldsymbol{D}} - \frac{2}{3}k\boldsymbol{I}\right) + \rho \boldsymbol{g} \qquad (3\text{-}8)$$

$$\boldsymbol{v} \cdot \nabla k = \nabla \cdot \left[\frac{1}{\rho}\left(\eta + \frac{\eta_t}{\sigma_k}\right)\nabla k\right] + 2\frac{\eta_t}{\rho}(\bar{\boldsymbol{D}} : \bar{\boldsymbol{D}}) - \varepsilon \qquad (3\text{-}9)$$

$$\boldsymbol{v} \cdot \nabla \varepsilon = \nabla \cdot \left[\frac{1}{\rho}\left(\eta + \frac{\eta_t}{\sigma_\varepsilon}\right)\nabla \varepsilon\right] + 2C_{1\varepsilon}\frac{\varepsilon}{k}\frac{\eta_t}{\rho}(\bar{\boldsymbol{D}} : \bar{\boldsymbol{D}}) - C_{2\varepsilon}\frac{\varepsilon^2}{k} \qquad (3\text{-}10)$$

$$\eta_t = C_\eta \frac{k^2}{\varepsilon} \qquad (3\text{-}11)$$

Where

v: is the velocity vector

k: is turbulent kinetic energy

D: is the rate deformation

ε: is the turbulent dissipation

η: is the fluid viscosity

η_t: is the eddy viscosity

The expression *(3-12)* represents the momentum equation, where $\frac{dv}{dt}$ is the accumulation term, $v \cdot \nabla v$ the convective term and $\rho \boldsymbol{g}$ represents the volume force.

$$\rho\left(\frac{\partial \boldsymbol{v}}{\partial t} + \boldsymbol{v} \cdot \nabla \boldsymbol{v}\right) = -\nabla P + \eta \nabla^2 \boldsymbol{v} - \rho \nabla < \boldsymbol{v}'\boldsymbol{v}' > + \rho\, \boldsymbol{g} \qquad (3\text{-}12)$$

Where P is the pressure and η is the fluid viscosity.

In this model it is assumed that the Rans approximation simplifies the Navier-Stokes equations by the use of average values of **v** and P instead of the instantaneous values. The problem is not closed, because of 6 additional variables. Using the Boussinesq's relation, it is possible to link Reynolds tensor to mean velocity v:

$$-\rho < \boldsymbol{v}'\boldsymbol{v}' > = 2\eta_t \bar{\boldsymbol{D}} \qquad (3\text{-}13)$$

The viscosity turbulence η_t has viscosity dimension and is a flow characteristic. Using Boussinesq's relation, the number of variables reduces from 6 to 1 (turbulent viscosity). Furthermore, a relation between η_t and **v** is added to the equation system.

The model chosen to solve this issue is the two equation model, which leads to the eq. from *(3-14)* to *(3-18)*.

$$\nabla \cdot \boldsymbol{v} = 0 \qquad (3\text{-}14)$$

$$\frac{\partial \boldsymbol{v}}{\partial t} + \boldsymbol{v} \cdot \nabla \boldsymbol{v} = -\frac{1}{\rho}\nabla P + \frac{\eta}{\rho}\nabla^2 \boldsymbol{v} + \nabla \cdot \left(2\eta_t \bar{\boldsymbol{D}} - \frac{2}{3}k\boldsymbol{I}\right) + \rho \boldsymbol{g} \qquad (3\text{-}15)$$

$$\frac{\partial k}{\partial t} + \boldsymbol{v} \cdot \nabla k = \nabla \cdot \left[\frac{1}{\rho}\left(\eta + \frac{\eta_t}{\sigma_k}\right)\nabla k\right] + 2\frac{\eta_t}{\rho}(\bar{\boldsymbol{D}} : \bar{\boldsymbol{D}}) - \varepsilon \qquad (3\text{-}16)$$

$$\frac{\partial \varepsilon}{\partial t} + \boldsymbol{v} \cdot \nabla \varepsilon = \nabla \cdot \left[\frac{1}{\rho}\left(\eta + \frac{\eta_t}{\sigma_\varepsilon}\right)\nabla \varepsilon\right] + 2C_{1\varepsilon}\frac{\varepsilon}{k}\frac{\eta_t}{\rho}(\bar{\boldsymbol{D}} : \bar{\boldsymbol{D}}) - C_{2\varepsilon}\frac{\varepsilon^2}{k} \qquad (3\text{-}17)$$

$$\eta_t = C_\eta \frac{k^2}{\varepsilon} \qquad (3\text{-}18)$$

Transport equations for standard k-ε model

The turbulence kinetic energy, *k*, and its rate of dissipation, *ε*, are obtained from *(3-19)* to *(3-30)* expressions:

$$\frac{\partial}{\partial t}(pk) + \frac{\partial}{\partial x_i}(pkv_i) = \frac{\partial}{\partial x_j}\left[(\mu + \frac{\mu_t}{\sigma_k})\frac{\partial k}{\partial x_j}\right] + G_k + G_b + \rho_\varepsilon - Y_M + S_k \qquad (3\text{-}19)$$

$$\frac{\partial}{\partial t}(p\varepsilon) + \frac{\partial}{\partial x_i}(p\varepsilon v_i) = \frac{\partial}{\partial x_j}\left[(\mu + \frac{\mu_t}{\sigma_\varepsilon})\frac{\partial \varepsilon}{\partial x_j}\right] + C_{1\varepsilon}\frac{\varepsilon}{k}(G_k + C_{3\varepsilon}G_b) - C_{2\varepsilon\rho}\frac{\varepsilon^2}{k} + S_\varepsilon \qquad (3\text{-}20)$$

In these equations, G_k represents the generation of turbulence kinetic energy due to the mean velocity gradients. From the exact equation for the transport of *k*, this term may be defined as:

$$G_k = -\overline{\rho v_i' v_j'}\,\frac{\partial v_i}{\partial x_i} \qquad (3\text{-}21)$$

To evaluate G_k in a manner consistent with the Boussinesq's hypothesis,

$$G_k = \mu_t S^2 \qquad (3\text{-}22)$$

Where *S* is the modulus of the mean rate-of-strain tensor, defined as:

$$S \equiv \sqrt{2S_{ij}S_{ij}} \qquad (3\text{-}23)$$

While G_b is the generation of turbulence kinetic energy due to buoyancy, calculated as described:

$$G_b = \beta g_i \frac{\mu_t}{Pr_t} \frac{\partial T}{\partial x_i} \quad (3\text{-}24)$$

Where Pr_t is the turbulent Prandtl number for energy and g_i is the component of the gravitational vector in the *i-th* direction. For the standard and realizable k-ε models, the default value of Pr_t is 0.85.
With

$$a_0 = \frac{1}{Pr} = \frac{k}{(\mu\ cp)}. \quad (3\text{-}25)$$

The coefficient of thermal expansion, *β'*, is defined as:

$$\beta' = -\frac{1}{\rho}\left(\frac{\partial \rho}{\partial T}\right)_p \quad (3\text{-}26)$$

For ideal gases, we have the reduction to:

$$G_b = -g_i \frac{\mu_t}{\rho Pr_t} \frac{\partial \rho}{\partial x_i} \quad (3\text{-}27)$$

Y_M represents the contribution of the fluctuating dilatation in compressible turbulence to the overall dissipation rate, calculated as described:

$$Y_M = 2\rho\varepsilon M_t^2 \qquad (3\text{-}28)$$

Where M_t is the turbulent Mach number, defined as:

$$M_t = \sqrt{\frac{k}{{c_i}^2}} \qquad (3\text{-}29)$$

Where c_i is the speed of sound

$$c_i = (\chi RT)^{0.5} \qquad (3\text{-}30)$$

Where χ is a constant.

3.2.3 Spray simulations

It is possible to simulate droplets dispersed in the continuous phase [33] using the *DPM model* implemented in Fluent. The trajectories of these discrete phase entities, as well as heat and mass transfer to/from them are computed. The coupling between the phases and its impact on both the discrete phase trajectories and the continuous phase flow can be included.

For liquid sprays, a convenient representation of the droplet size distribution is the Rosin-Rammler expression. The complete range of sizes is divided into an adequate number of discrete intervals; each represented by a mean diameter for which trajectory calculations are performed. If the size distribution is of the Rosin-Rammler type (Y_D), the mass fraction of droplets of diameter greater than D_p is given by:

$$Y_D = e^{-(D/\bar{D})^n} \qquad (3\text{-}31)$$

In *Table 3-2* are resumed the parameters used for Rosin-Rammler model:

Parameter	**Value**
Spread number	**3.5**
Min. diameter	50 µm
Max diameter	750 µm
Mean diameter	350 µm

Table 3-2 Parameter for Rosin-Rammler distribution

The quantity $\bar{D}$ is the *Mean Diameter* and to *n* is the *Spread number.*

The trajectory of a droplet is calculated by integrating the force balance on it, which is written in a Lagrangian reference frame[34]. This force balance equates the particle inertia with the forces acting on the particle, and can be written as:

$$\frac{d_{v_{droplet}}}{d_t} = F_D\left(v - v_{droplet}\right) + \frac{g(\rho - \rho_{droplet})}{\rho_{liq}} + F_i \qquad (3\text{-}32)$$

Where

F_i is the Termophoretic force

v is the fluid phase velocity

$v_{droplet}$ is the droplet velocity

ρ is the fluid density

$\rho_{droplet}$ is the droplet density

g is the gravitational term

$F_D\ (v - v_{droplet})$ is the drag force per unit particle mass:

$$F_D = \frac{18\mu}{\rho_{droplet} D^2}\frac{C_D Re}{24} \qquad (3\text{-}33)$$

Where

Re is the Reynolds number evaluated as $Re = \frac{\rho\, D\, |v_{droplet} - v|}{\mu}$

D is the droplet diameter

μ is the molecular viscosity of the fluid

C_D is the drag coefficient.

3.3 Post processing

The WES fluid dynamic is showed in terms of droplets trajectories (*Fig. 3-8*), gas streamlines (*Fig. 3-9* and *3-10*) and droplets velocity along the column. Two simulations were performed using the input parameters the reported in *Table 3-3*:

	Gas flow rate [m^3/hr]	**Liquid flow rate [m^3/hr]**	**T gas [K]**	**T liquid [K]**
Case 1	140	195	323	300
Case 2	125	195	323	300

Table 3-3 Input parameters

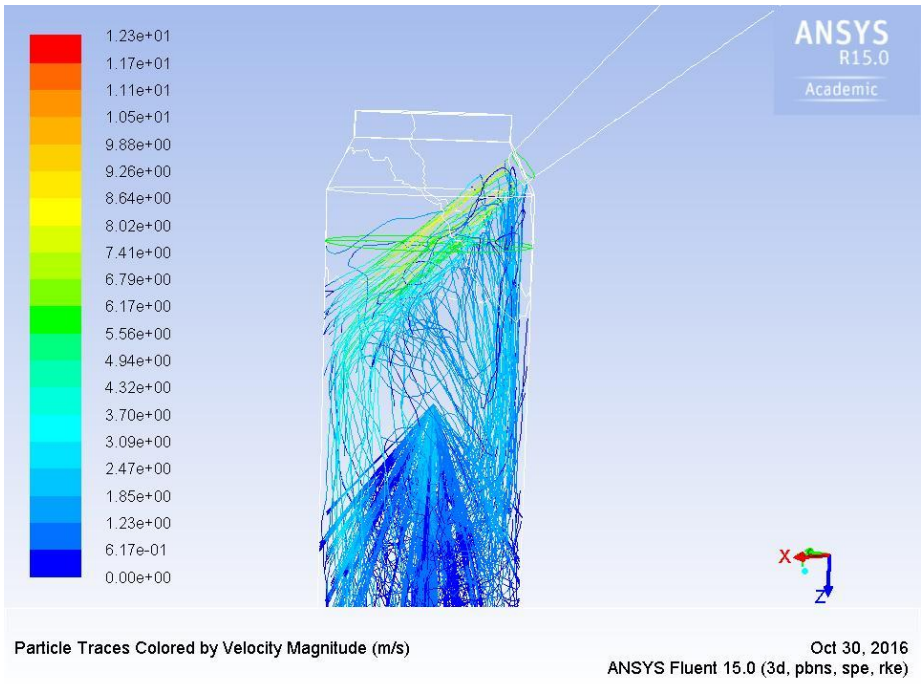

Figure 3-8 CFD streamlines of the spray water injection

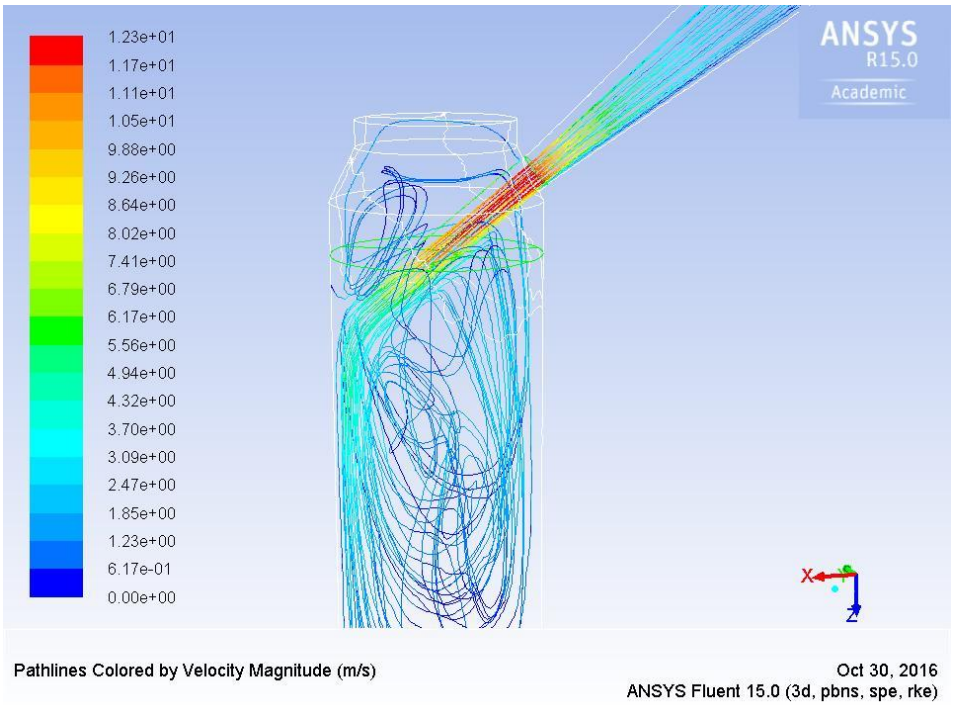

Figure 3-9 Details of sample CFD streamlines of massless particles surface injection used for gas streamlines tracking

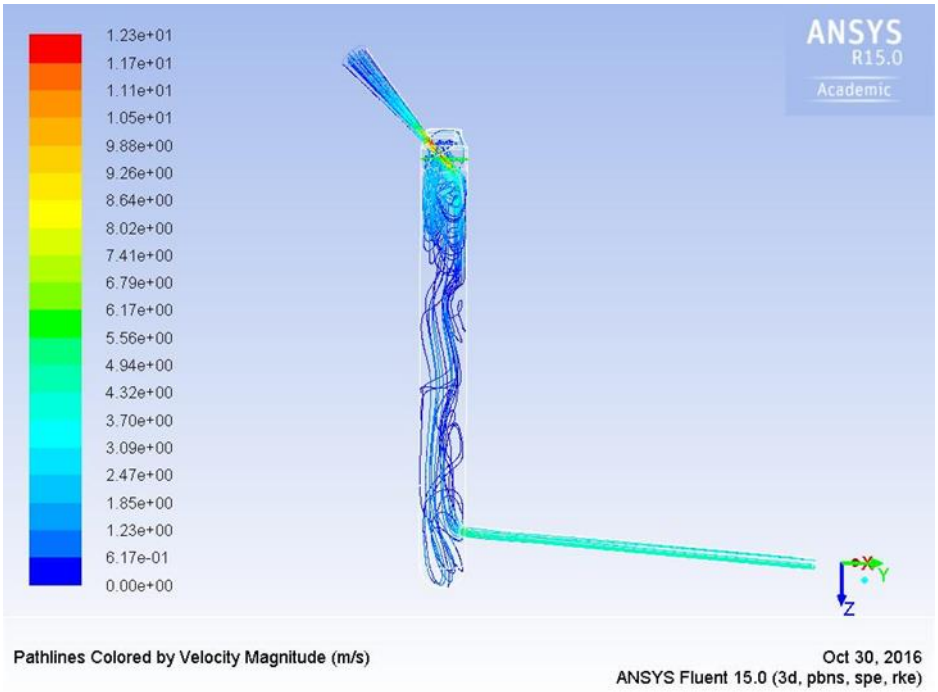

Figure 3-10 Sample CFD streamlines of massless particles surface injection used for gas tracking

By dividing the WES column in 74 sub volumes, using 75 horizontal surfaces perpendicular to the gas flow direction (*Fig. 3-11*), the droplets distribution $\psi(D)$, their concentration, N and their velocity along the column should be determined to apply the particle capture model.

On each surface the number of droplets (for each droplet size) and their velocity were gathered from *Fluent* and the arithmetic average value of these variables of two consecutives surfaces is assumed to be representative of the volume average values of each variable.

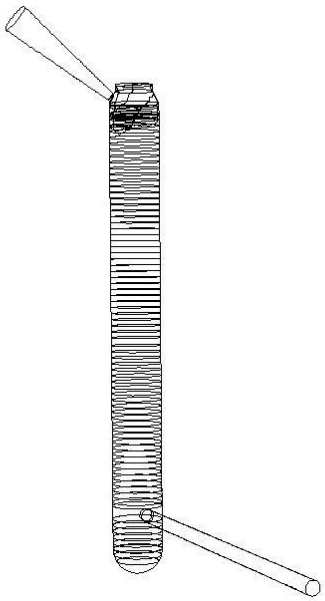

Figure 3-11 Scrubber volume division by 75 planes

To determine the gas residence time, the surface injection was used as follows. The inlet section of the scrubber was divided in *n* subsection (the mesh cells in that section, 189 in this study). From the center of each element of the inlet surface, a massless particle is added and its path-lines were followed through the WES. This allows to cover every possible path achieved by the gas entering the scrubber, and, neglecting the particles inertia (usually tested particles are smaller than 500 nm), this approach can be used as a particle tracking procedure (*Fig. 3-12*). Each streamline will give rise to a given residence time, from which a general residence time distribution can be eventually determined. The streamlines can be proficiently used to determine the actual time that all particles moving along a streamline pass in the 74 sub-volumes in which we calculated the particle capture efficiency.

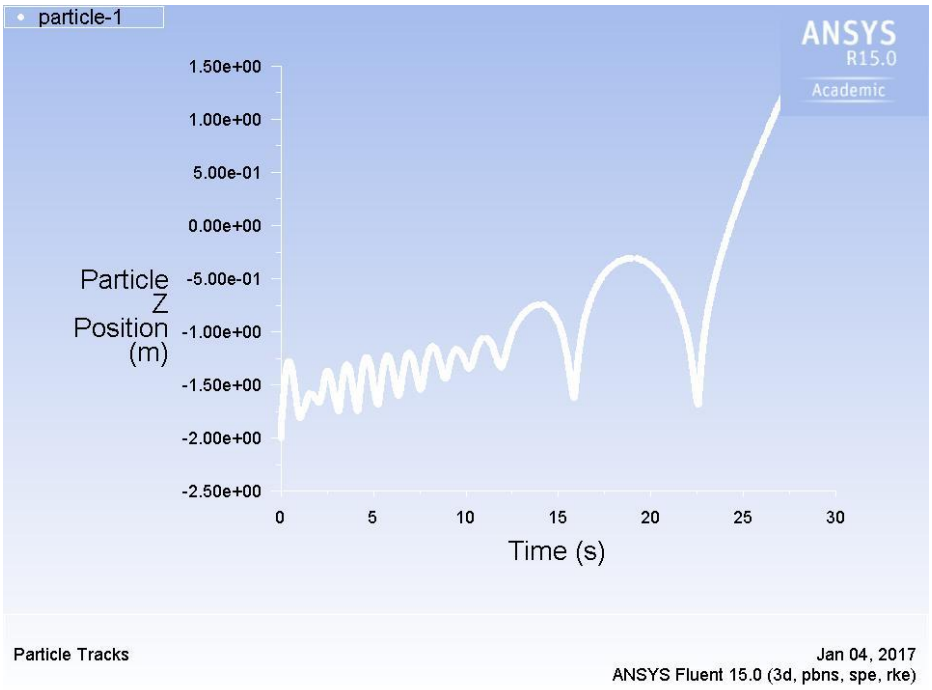

Figure 3-12 Example of particle tracking plot for one stream-line

The fluid dynamic information acquired in post processing were used in *Matlab* to evaluate the particle capture model described in *Chapter 1.2*.

For each droplet diameter *i*, on each *k-th* surface, $N_{drop,k}$ number of droplets, U_k (D_i) were gathered and the average value of these variables of two consecutives surfaces is assumed to be representative of the volume average values of each variable.

On each *k-th*, droplets distribution $\Psi_k(D_i)$ is evaluated (*eq. (3-34)*):

$$\Psi_k(D_i) = \frac{\pi D_{i,k}^3}{6}\frac{1}{l_{i,k}^3} \qquad (3\text{-}34)$$

That is the droplets volume $V(D_{i,k})$ between two planes (*eq. (3-35)*).

$$V(D_{i,k}) = \Psi_k(D_i) S \Delta z \qquad (3\text{-}35)$$

The variable $l_{i,k}$ is the distance between two droplets under the hypothesis that they are arranged in cubic with centered face configuration, 10 is the number of tries, a parameter that includes the turbulent velocity fluctuations in the particle force balance (eq. (*3-36)*).

$$l_{i,k} = \sqrt{\frac{Area_{column}}{10\ N_{i,k}}} \qquad (3\text{-}36)$$

The volumetric droplet concentration $N_{i,k}^3$ is also calculated (*eq. (3-35)*):

$$N_{i,k}^3 = \frac{1}{l_{i,k}^3} \qquad (3\text{-}37)$$

This allows the estimation of E_k $(D_{i,k}, d_{p,k})$ collisional efficiency, $Q_{d,k}$ $(D_{i,k})$ charge on droplets values per each volume.

According to the capture model, following the numerical *Matlab* function, the *k-th* volume collisional efficiency (*3-38*) for the *i-th* droplet diameter and for a given particle diameter ($d_{p,k}$) is estimated as:

$$\Lambda_{i,k} = E_{i,k} S_{i,k} U_{i,k} N_{i,k}^3 \qquad (3\text{-}38)$$

Where $E_{i,k}$ is the sum of electric$E_{electric,i,k}$, inertial impaction $E_{inert,i,k}$, directional forces $E_{dir,i,k}$, Brownian motion $E_{brown,i,k}$ (*eq. (3-39)*):

$$E_{i,k} = E_{electric,i,k} + E_{inert,i,k} + E_{dir,i,k} + E_{brown,i,k} \qquad (3\text{-}39)$$

The electric contribute is divided in other parts (*eq. (3-40)*):

$$E_{electric,i,k} = E_{coulomb,i,k} + E_{cd,i,k} + E_{cp,i,k} \qquad (3\text{-}40)$$

Where E_{cd} and E_{cp} are the efficiencies due to the image charges respectively on droplets and particles. The scavenging coefficient $\Lambda_{TOT,k}$ is calculated for each sub volume (*eq. (3-41)*), considering all the droplet diameters in the system:

$$\Lambda_{TOT,k} = \sum_{i=1}^{num\_drop} \Lambda_{i,k} \qquad (3\text{-}41)$$

At this point, in order to evaluate the particle capture efficiency, the residence time is needed.
As described above, 189 possible paths should be considered, therefore the residence time is represented as matrix having as rows the number of volumes (*k*) in which the reactor is divided and 189 columns as the path-lines tracked. If *j* is the path-line subscript, it is clear that, time is an information acquired as ratio of the position of *j-th* line and its velocity in the volume limited by *k* and *k+1*. a particle with a d_p diameter could follow *j*=1 *to* 189 path-lines are considered. Having all data available, the efficiency $\eta_k(d_p)$ for each generic *k-th* sub volume is estimated as reported in *eq (3-42)*:

$$\eta_{k,j}(d_p) = 1 - \exp(-\Lambda_{TOT,k} \mathrm{t}_{k,j}) \qquad (3\text{-}42)$$

The same formula can be used to determine the number of particles of size d_p leaving the volume *k*, which is given by:

$$n_{k,j}(d_p) = n_{k-1,j}(d_p) \cdot \sum exp(-\Lambda_{TOT,k} t_{k,j}) \qquad (3\text{-}43)$$

Using this approach along a streamline will provide the particle depletion from the inlet plane (concentration $n_{0,j}(d_p)$) to the exit plane (concentration $n_{74,j}(d_p)$). The concentration $n_{0,j}(d_p)$ is given by dividing the inlet concentration $n_0(d_p)$ by the number n of cells in which the inlet section was divide (189 in our case). The particle of size d_p leaving the WES column are given by the sum of particles leaving each of the streamlines and the overall removal efficiency is given by:

$$\eta(d_p) = 1 - \frac{\sum_{j=1}^{n} n_{74,j}(d_p)}{n_0(d_p)} \qquad (3\text{-}44)$$

Once the model equations were set up, the actual calculation of particle capture required the assessment of particle charge, which is achieved following the so-called *Aerosol current approach*. On the other hand, the model equation can be used to obtain information on the actual particle charge required to achieve a certain removal efficiency under given experimental conditions. This approached is called *Particle charge distribution approach*. The two approaches are described thereinafter.

3.3.1 Aerosol current (AC) approach

The charging model of Porteiro et al. [25] described in *Chapter 2* was used for the capture model. The theoretical mean charge carried by each particle, was calculated as reported in (*eq. (3-45)*):

$$q_{tot} = q_{field} + q_{diff} \qquad (3\text{-}45)$$

Where q_{field} and q_{diff} are evaluated according to *(3-46)* and *(3-47)*:

$$q_{field} = \frac{q_s\left(\frac{t_r}{\tau}\right)}{1+\frac{t_r}{\tau}} \qquad (3\text{-}46)$$

$$q_{diff} = \frac{d_p k_B T}{2k_e e} \, ln\left[1 + \frac{\pi K_e d_p c_i e^2 N_i t_r}{2k_B T}\right] \qquad (3\text{-}47)$$

These formulas require the evaluation of the ion concentration, N_i, *eq. (3-48)*:

$$N_i = \frac{I_{Mod}}{eEAZ_i} \qquad (3\text{-}48)$$

I_{Mod} (*eq. (3-49)*) is the current supplied by the high voltage generator that was estimated according to Yamada [35], who extend the validity of the classical Townsend formula for electric discharge to predict the effect of temperature and geometry of the charger:

$$I_{Mod} = \beta_1 \, V(V - V_0) \qquad (3\text{-}49)$$

Where

β_1 is a correcting factor related to system geometry

V is the applied voltage

V_0 is the voltage at which the corona discharge occurs

Adapting the *eq. (3-49)* to the particle charge geometry of the case study, a new correcting factor β_1 is considered. This value depends on PCU geometry and operating conditions and is obtained comparing the I_{MOD} with experimental current available data. Since the ionic concentration is a function of the current, it is possible to write:

$$N_i = \beta_1 \frac{V(V-V_0)}{eEAZ_i} \qquad (3\text{-}50)$$

At this point, for every particle diameter the charge is estimated. As reported in *Chapter 1* in *Table 1-3*, particle charge is used to determine the electric collisional efficiency and it is possible to obtain for each *k* volume the particle capture efficiency.

3.3.2 Particle charge distribution (PCD) based approach

A statistical approach is proposed: when there is a corona source fixing a particle diameter d_p, a Gaussian charge distribution should be considered for each class of particles. Instead of using the Gaussian distribution, due to the discrete nature of electric charges, the Binomial distribution was adopted.

The binomial distribution with parameters *n* and *p* is the discrete probability distribution of the number of successes in a sequence of *n* independent yes/no experiments, each of which yields success with probability *p*. In general, if the random variable X follows the binomial distribution with parameters n ∈ ℕ and p ∈ [0, 1], is possible to write X ~ B(n, p). The probability of getting exactly *y* successes in n trials is given by (*eq. (3-51)*):

$$f(y; n, p) = \Pr(X = y) = \binom{n}{y} p^y (1-p)^{n-y} \qquad (3\text{-}51)$$

And the mean value of the distribution is calculated directly:

$$mean = \sum_{i=1}^{n} x_i p_i \qquad (3\text{-}52)$$

In this work $p \in [0, 1]$ and n=1000 items. Each item of *p* provides a profile of the binomial curve (*Fig. 3-13*).

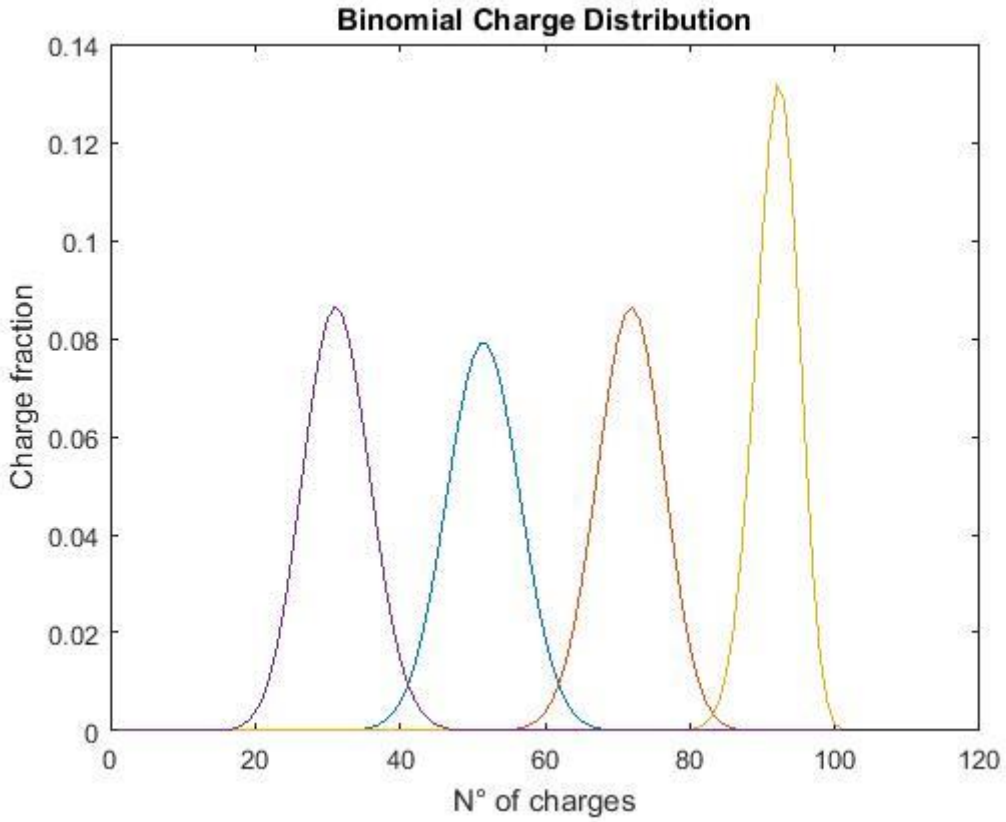

Figure 3-13 Binomial charge distribution. Number of charges=100, violet for p=0.3; green for p=0.5; red for p= 0.7; yellow for p=0.9.

Through the statistic approach we can keep the value of n fixed to *n=1000*, the parameter *p* is evaluated that gives back the binomial distribution (ψ) value that allows the best-fitting with the total efficiency, for each particle diameter.

$$\psi(p, d_p) = \binom{1000}{y} p^y (1-p)^{1000-y} \qquad (3\text{-}53)$$

For each particle diameter d_p a certain binomial charge distribution is associated. Particle capture efficiency at each surface *k* is estimated as follows. The only parameter to evaluate is the parameter *p*, it is calculated as follows:

$$\eta_k(p, d_P) = 1 - \psi(p, d_p)(\exp(-\Lambda_k(d_p)\, t_{res,k})) \qquad (3\text{-}54)$$

$\psi(p, d_p)$ does not depend on the other parameters and can be taken out from the exponential.
Out of the WES (at k= *75*) $\eta_{out\_binomial}$ is evaluated for each particle diameter, depending on *p*. Once evaluated $\eta_{out\_binomial}$ is compared to $\eta_{experimental}$ value and a minimum function is calculated. The only variable in this function *g(p)* is the shape-parameter *p* (*eq. (3-55)*):

$$g(p) = |\eta_{experim} - \eta_{out\_binomial}(p)|^2 \qquad (3\text{-}55)$$

Therefore, the mean statistic charge on each diameter using the binomial mean formula is (*eq. (3-56)*):

$$q_{binomial}(dp) = \sum \psi(d_p) \qquad (3\text{-}56)$$

And the load current (*eq. (3-57)*):

$$I_{binomial}(dp) = q_{binomial}(dp) Q_{gas} e n_0(dp) \qquad (3\text{-}57)$$

Where n_0 is the initial numeric concentration of particles [#/m^3] of size d_p entering the wet electrostatic scrubber. Q_{gas} is the volumetric flow rate [m^3/s], *e* is the elemental electric charge [C]. Using this approach it is possible to obtain:

- The number of charges on each particle with a diameter d_p;
- The currents on the particles.

3.4 Results and discussion

PCD based model has shown considerable strength varying gas flow rate and operative electric parameters. Furthermore, through this evaluation the AC approach limits were shown. PCD approach relates the efficiency directly to the charge acquired by particles through the binomial parameter *p*. To better understand the differences between PCD and AC model, in *table 3-4* are reported as example one operating condition of experimental campaign for *DEECON* project. Results of PCD and AC approaches for *LAS* data at V_{PCU}= - 15 kV and V_{ES}= - 15 kV are shown in *Fig. 3-14*. It appears clear that there are some incongruities between AC model and experimental data, even trying to adjust the ion concentration with a fitting parameter β_1.

Several experimental tests were carried with this pilot, as described in *Chapter 3.1*, but for simplicity, one experimental condition will be reported (*Table 3-4*).

L [lt/hr]	*G [m^3/hr]*	*V_{DCU} [kV]*	*V_{PCU} [kV]*	*I_{PCU} [μA]*	*η_{TOT}, (LAS)*
195	*140*	*15*	*15*	*200*	*0.89*

Table 3-4 Experimental conditions of one test carried out on WES Deecon

In *Fig. 3-14* the results and comparisons between the AC and PCD models are shown. The discrepancies existing in number of charges affect the capture efficiency. It is clear that for AC model even with the correcting factor β_1, it is not possible obtaining a good match with experimental data, in spite of PCD model.

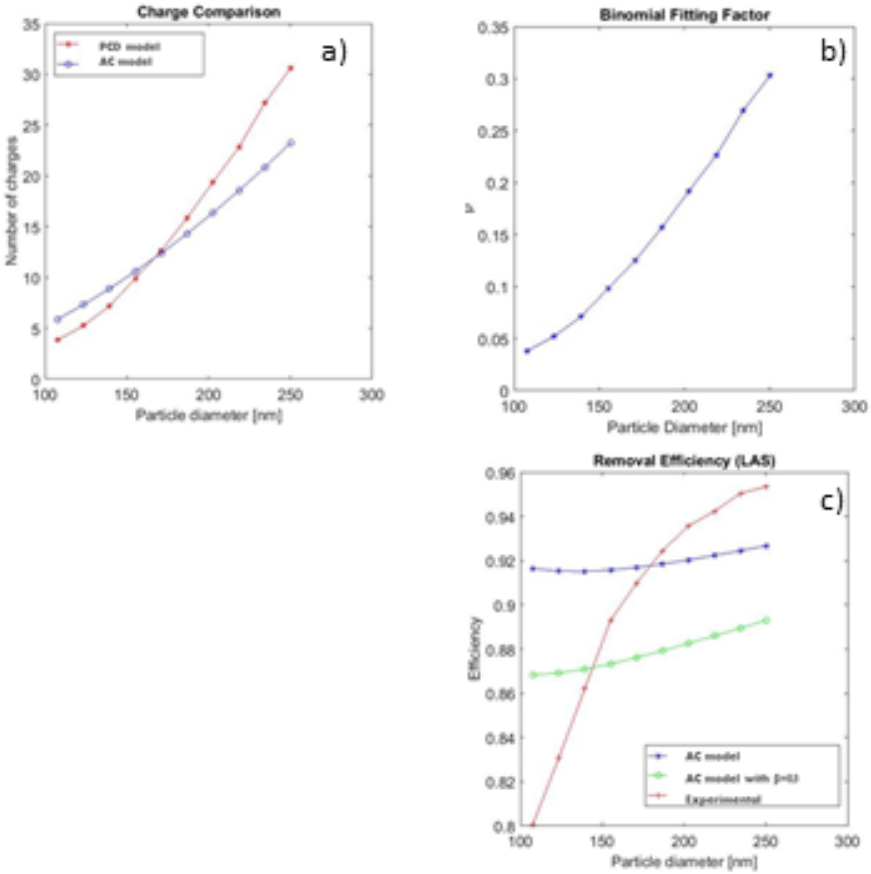

Figure 3-14 AC and PDC models comparison. a) Number of charges vs particle diameter; b) p (binomial factor) vs particle diameter; c) Particle capture efficiency for AC model, AC model with the fitting factor β_1 and experimental vs particle diameter.

Even if there is not a good match in terms of particle capture efficiency, the current carried by charged particles was evaluated and compared.

It is clear that even if in terms of total particle capture efficiency AC model is not able to predict the experimental data, it presents a good match with current values, but as well as PCD model that shows its validity even for this evaluation *(Table 3-5).*

L=195 kg/h, V_{ES}=15 Kv	V_{PCU}, kV	G, m^3/h	I_p, µA	Total Capture efficiency
Experimental	*15*	*140*	*84*	*0.89*
AC model			*84*	*0.876*
PCD model			*88*	*0.89*

Table 3-5 Total capture efficiency and current for AC, PCD approaches and experimental data

For all the experimental tests carried out on *Deecon* WES, that means changing PCU and ES voltages and gas flow *p* values are compared. In *Fig. 3-15 p* values are obtained comparing experimental and modelled efficiencies.

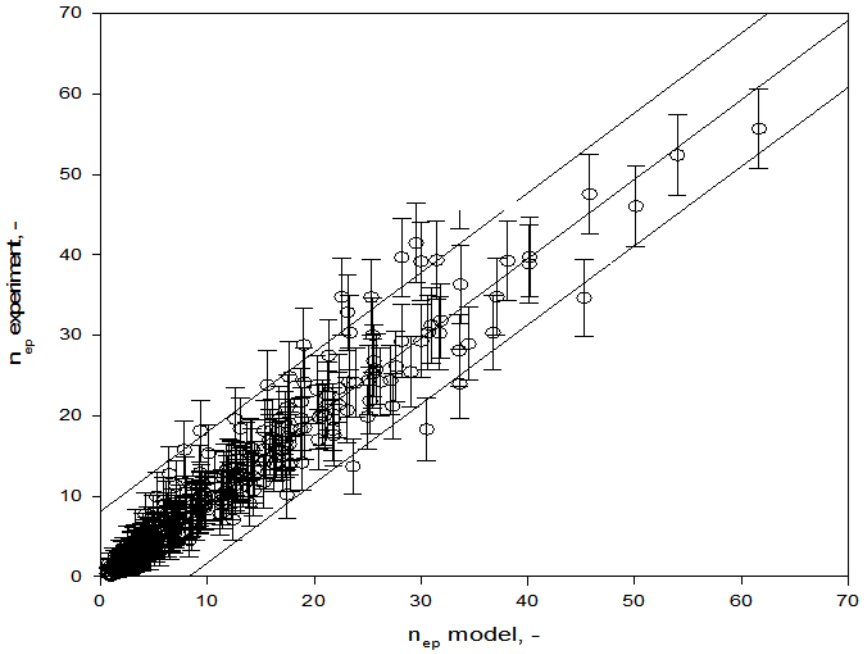

Figure 3-15 p values comparing η_{exp} vs $\eta_{PCD\ model}$

All the values of *p* are consistent and a relation with the applied voltage and the particle diameter is obtained (*eq. (3-58)*):

$$q(d_p)_{avg} = a \cdot d_p^b \cdot V^c \qquad (3\text{-}58)$$

Where *a b* and *c* are geometrical parameters, depending on PCU geometry and electrodes.

$$a = (1.364 \pm .506) \cdot 10^{-7} \qquad (3\text{-}59)$$

$$b = (2.749 \pm 0.062) \qquad (3\text{-}60)$$

$$c = (1.469 \pm 0.055) \qquad (3\text{-}61)$$

In *eq. (3-58)*, the mean value of the electric charge $q(d_p)_{avg}$ is reported, depending on particle size and applied voltage. Regarding at *table 2-6*, it is clear that the main difference between the two models is in term of particle capture efficiency. In terms of particle current, both of PCD and AC model give a good match with experimental values, but for capture efficiency, PCD model gives a better fitting. Since the electrical variables (electric field, ion concentration, charging time…) also depend on charging geometry system, the *eq (3-58)* takes into account these parameters.

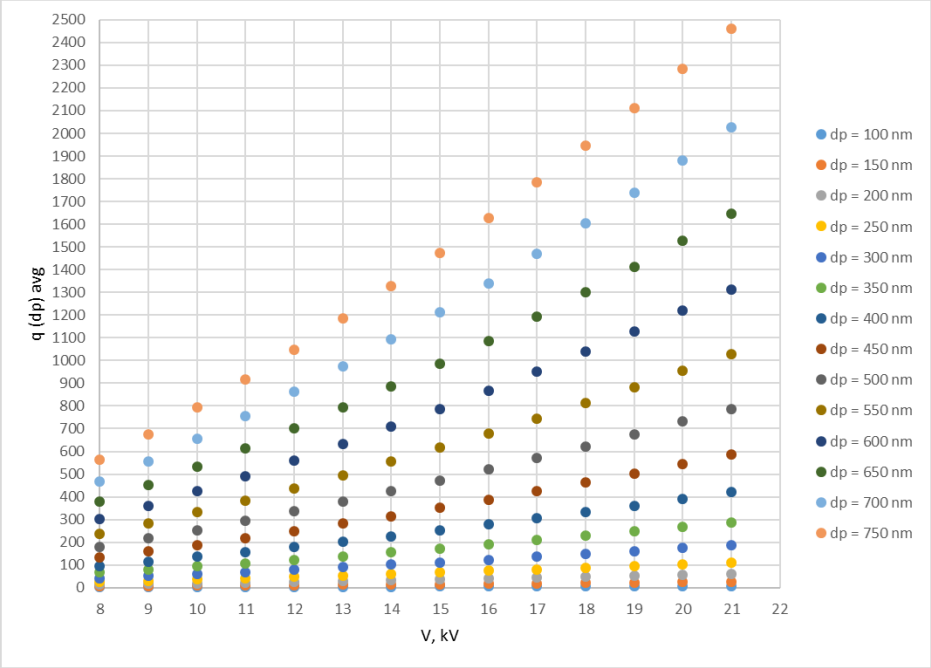

Figure 3-16 Mean charge vs Voltage according to eq. (2-51)

In *Fig. 3-16* the average charge of particles vs applied voltage is reported. This evaluation gives back the amount of charge, fixing a certain particle diameter. In this way, you can predict the number of charges for a certain PCU system. This expression gave information about the applied

voltage that should be used for an another PCU system, having a similar geometry and used for the design of a new WES system, explained in detail in *Chapter 4*.

In *Fig. 3-17* the comparison between the experimental efficiency of *DEECON* case study and the theoretical efficiency estimated by calculating the particle charge by means the PCD model.

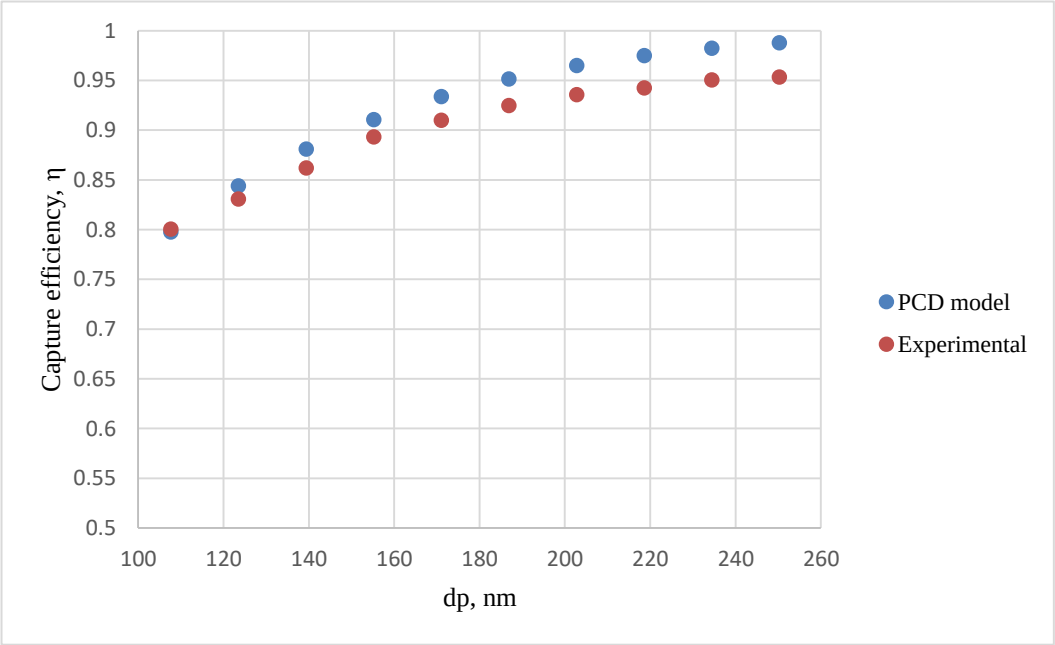

Figure 3-17 Comparison between experimental and theoretical efficiencies

As it can be seen in *Figure 3-17*, the experimental results are well described by the capture efficiency evaluated by using the PCD model. It means that the model allows us to predict the minimum voltage (V=10 kV) to obtain a 90% of capture efficiency for a given range of particle diameter. This result was used to design a WES system operating at higher gas flow rates (ranging from 5500 to 10000 Nm^3/h).

Chapter 4. Design, set up and testing on the pilot scale WES at the Boldrocchi s.r.l.

In this chapter, the experimental apparatus of WES pilot is presented. It was realized in collaboration with Boldrocchi s.r.l. group. In this system gas and liquid are in cross-flow. Particles are carried by gas and pass through the PCU that is made up of ten lines of needles.

Liquid is sprayed by 41 hollow cones nozzles. This WES pilot worked at different conditions of gas and liquid flow, changing ES and PCU voltages. All the experimental materials and data are reported in this chapter. As described in *Introduction*, WES system is made up of a particle charging unit and a set of 41 electrified spray nozzles, which for intellectual properties rights are not shown here.

For what concerns the contact chamber, a preliminary evaluation was realized through the computational software *Ansys Fluent*. Starting from Di Natale et al. [7] a point of start was established to estimate liquid and gas flowrate for the prototype. The liquid/gas ratio is about 2 kg/kg and under the hypothesis of 5000 m^3/h of gas flow rate, the liquid flow rate is about 10 m^3/h.

The dimension of the reactor depends on the following peculiarities/prerequisites:

- The apparatus should be transportable;
- The chamber dimensions have to guarantee an optimal contact between liquid and gas phases;
- The ES on the roof was arranged according to nine lines, at a distance optimum to avoid interferences among neighboring spray. In order to obtain the desired liquid flow rate, 41 units operating at 3.9 l/min liquid flow as maximum.

Taking into account these considerations, the WES dimensions are gained: 4 m as length, weight of 1.5 m and high 2 m.

Gas velocity profile is studied with *Ansys Fluent*. Three grids are arranged in the divergent inlet channel in order to avoid the entrance effect and one in the convergent to decelerate the velocity in outlet. In *Fig.4-1* is reported the velocity field of the final configuration of WES system.

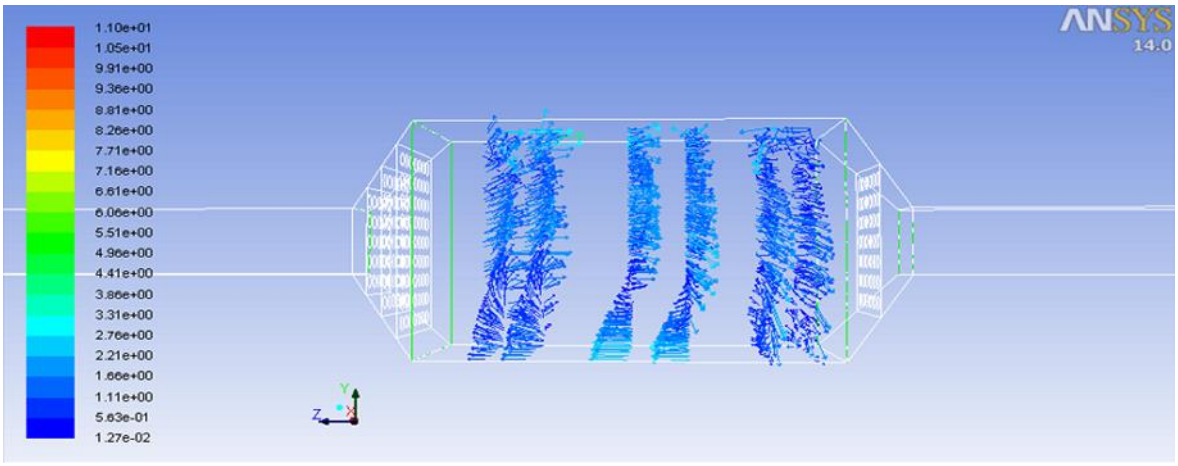

Figure 4-1 Velocity field of contact chamber simulation

4.1 Materials and methods

In *Fig. 4-2* the P & ID is shown.

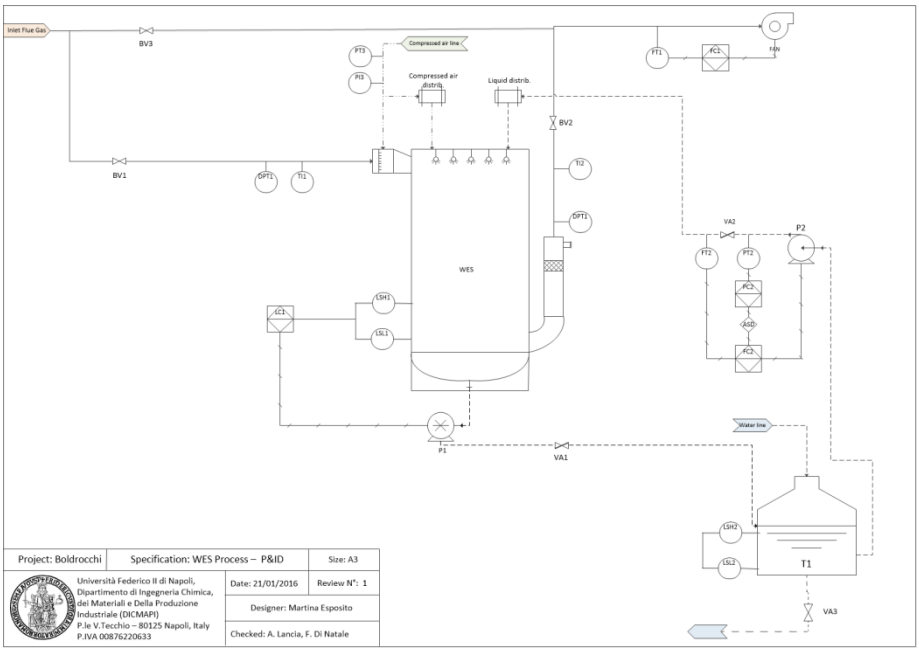

Figure 4-2 P & ID prototype plant WES. TI1: temperature indicator IN the reactor; TI2: temperature indicator OUT the reactor; LSH1: upper water-level sensor in the WES; LSL1: lower-water level sensor in the WES; T1: water tank; LSH2: upper-level sensor of water in the tank; LSL2: lower-level tank sensor of water in the tank; DPT1: indicator of pressure drop in the reactor; P1: drain pump; P2: supply pump; BV1-BV2-BV3: shutters; VA1: control valve for the drain pump; VA2: regulating valve for supply pump; VA3: regulation valve for water tank; PT2: pressure transducer for supply pump; PC2: pressure controller for supply pump; FC2: flow controller for supply pump; FT2: transducer for the supply pump; LC1: level signal control for WES; FT1: flow transducer; PI3: pressure indicator for compressor; PT3: pressure transducer for compressor.

The above-mentioned charging systems are so arranged: the PCU is located before the contact chamber between, the gas first passes through this unit allowing the submicronic and ultrafine particles to charge and then enters in the contact chamber. Here it meets in crossflow the liquid, sprayed by the ES placed on the roof of the chamber. In *Fig. 4-3* is shown a photograph of the prototype.

Figure 4-3 Wet Electrostatic Scrubber prototype

The plant is equipped with control systems, described in detail in *Chapter 4.1.1*.

The system provides the following lines: water line, compressed air line and the electric one.

The water line begins at the storage tank T1 where the liquid is sent through the delivery pump P2 to the 41 nozzles. Water flows into a main pipe and is sent to five conducts connected to the main line through five electro-valves. Furthermore, on-off valves give the opportunity to manually regulate the water in the pipes. Once the liquid has been sprayed by the nozzles in the chamber WES, it comes into contact with the gas and reaches the bottom of the chamber. Water is transferred, together with the capture-particles, into sewer by the drain pump P1.

Compressed air is necessary for the cleaning of electrical devices. Part of the air is supplied to the ES and part for the PCU.

The electric circuit is necessary for PCU and ES. PCU is connected to a high voltage generator (*Spellman- SL2KW*), while the ES are supplied by three separated generators (*Spellman-*

PTV20N200). In *Fig. 4-4* the high voltage lines and the hydraulic ones are sketched. The details of the high voltage generators are reported in detail in *Chapter 4.1.1*.

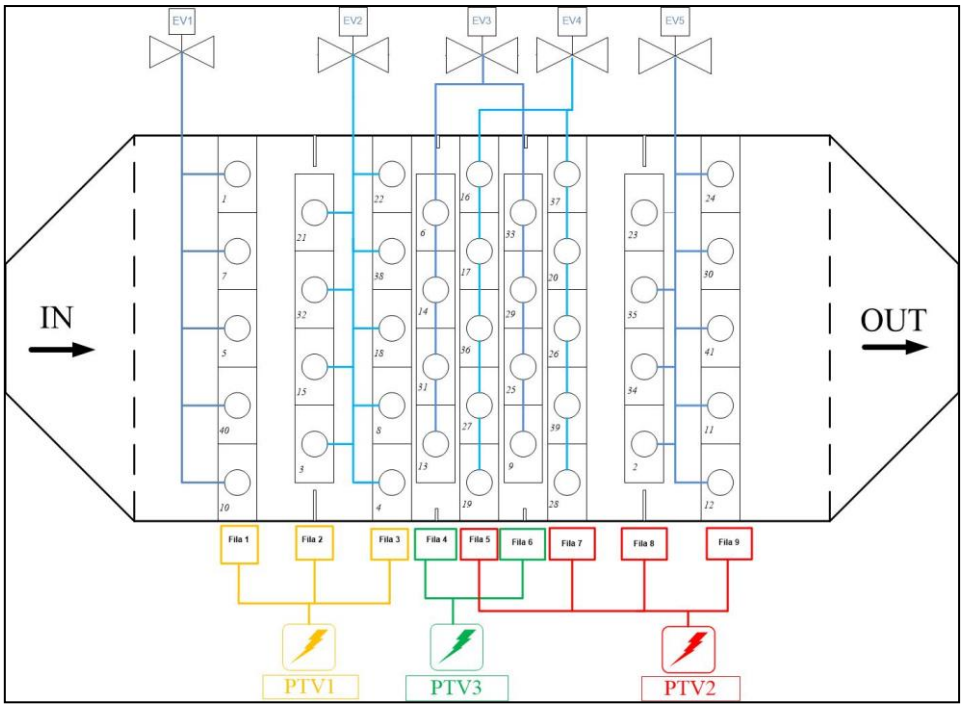

Figure 4-4 Electric and hydraulic scheme.

4.1.1 Auxiliary equipment

- High voltage generators for particle and water charging
    - *Spellman* - SL2KW (*fig. 4-5*): PCU supplier. The maximum power supplied is 2 kW, with a maximum voltage of 30 kV and 66.6 mA of current. This generator has a reversible polarity, but it is used just for negative one.

Figure 4-5 SL2KW Generator

- *Spellman* - PTV20N200 (*fig. 4-6*): ES generator. These devices have a negative polarity, with a maximum power of 200 W. The maximum voltage that are able to supply is 20 kV and 10 mA of current.

Figure 4-6 PTV20N200 Generator

These devices were modified in order to deal with sparks formation both for PCU and ES. In particular, when a spark occurs in the system, PTVs have to keep the voltage (because the internal arc rate was modified) while the SL has to shut off.

- Drain and supply pumps.
    - *Lowara* - 10SV21P110T (*Fig. 4-7*). The supply pump was chosen because of the liquid flow (maximum 10 m^3/h) and the prevalence.

Figure 4-7 Supply pump

- *Lowara* - SHOE 25-125/22 (*fig. 4-8*). The drain pump has an important characteristic: it is able to work with dirty water, so with suspended solids.

Figure 4-8 Drain pump

In order to evaluate the capture efficiency, particle flow out the WES is characterized through the analyzer *TSI 3340*. The sample point was realized in the out duct, where a 6 mm tube was connected. Then, the gas stream passes first through two *PALAS VKL 10* series diluters (*Fig. 4-9*), a *TSI 3087* neutralizer (*Fig. 4-10*) and before entering the analyzer.

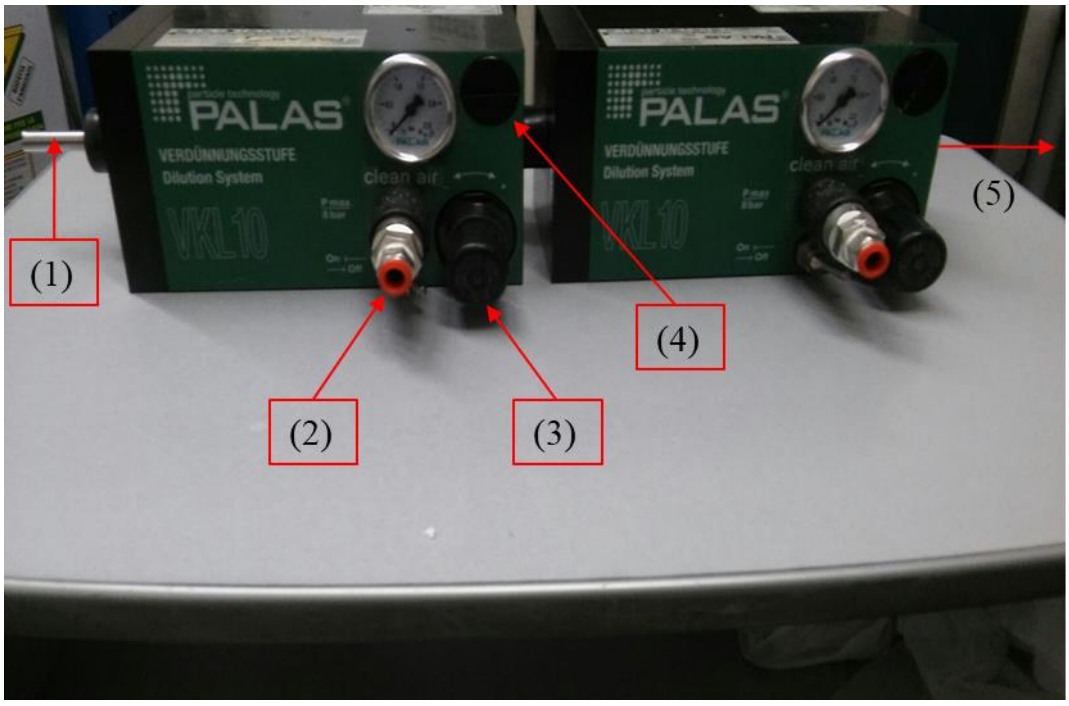

Figure 4-9 Diluters. 1) Inlet sample gas flow (coming from WES); 2Diluting air inlet; 3) regulating valve; 4Diluted air outlet; 5) Outlet sample gas flow

The *diluters* (f*ig. 4-9*) use dilution air at 6 bar to dilute the gas flow containing sample particles. They force a dilution factor of 10, i.e. a total factor of 100 considering their application in series. They are characterized by two inlets for compressed air, inlet and outlet for air in excess, an inlet and outlet for the sampling gas. Through these devices it is possible to regulate the aspiration rate in order to guarantee the isocinetism between the WES duct and duct of the dilutors. The *neutralizer* (*Fig. 4-10*) has the role to remove the residual charge on particles to avoid interferences with the analyzer.

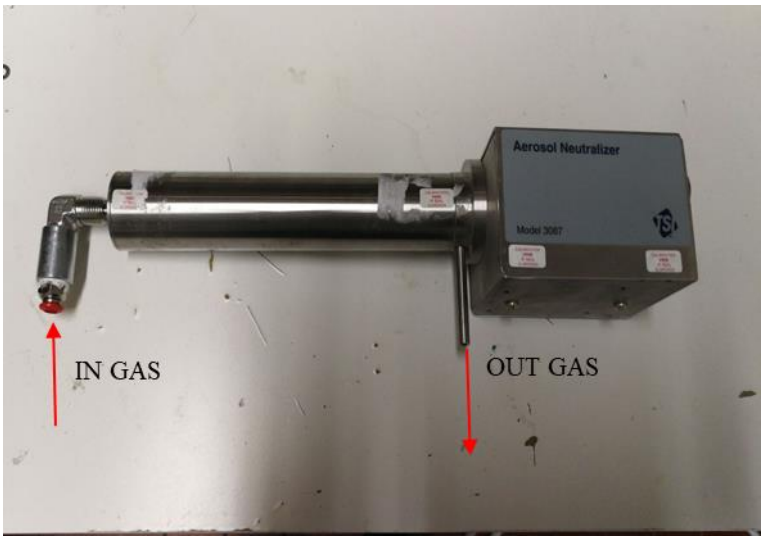

Figure 4-10 Neutralizer

The system was monitored by a software connected to the "Programmable Logic Controller" PLC control system. The graphic interface of the software is shown in *Fig. 4-11*. This software allows to perform these operations:

• Opening and closing of electrovalves;
• Regulation of fan.
• Activation of Supply pump;
• Activation and regulation of applied voltage to ES and PCU;
• Level control of the liquid in WES chamber
• Activation of particle generation system and dust load regulation;

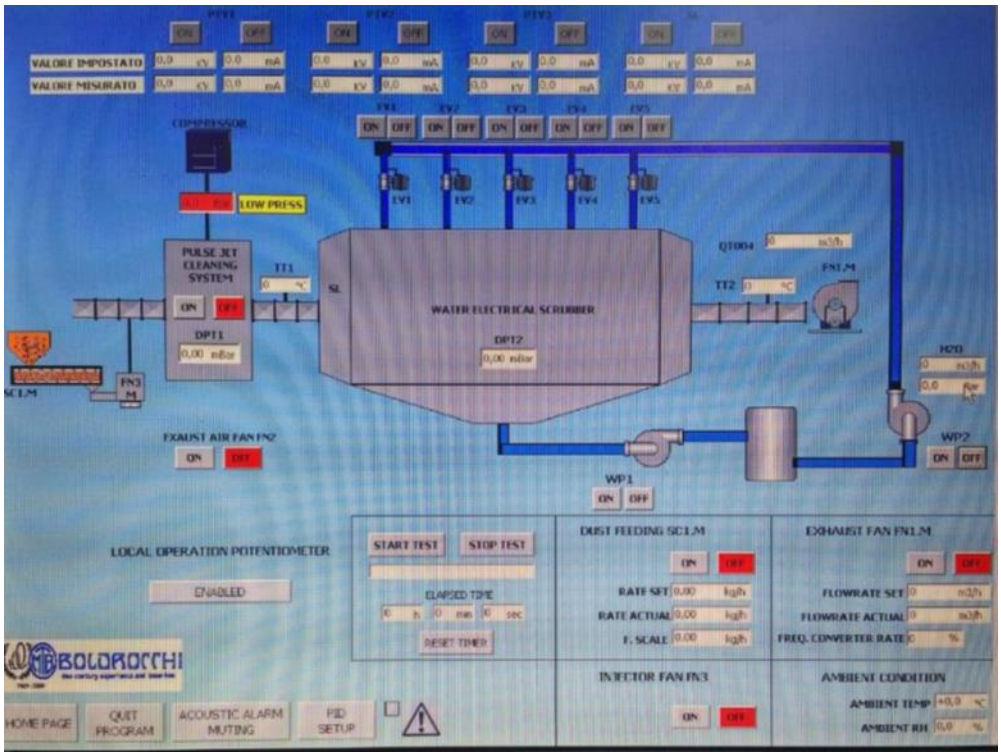

Figure 4-11 Graphic interface of PLC for the PILOT SCALE unit

4.2 Experimental procedure

4.2.1 Preliminary tests

Several preliminary tests were taken in order to verify the correct operating conditions of the PCU, and establish the optimal values for ES systems voltages.

- *Test on PCU operating conditions:* in absence of particles in inlet, the PCU voltage was changed until the breakdown value was reached. At this value, arcs appear in the system and the maximum operating value for the devise was fixed. The test was carried out setting three gas flows between 5500 and 10000 m^3 / h.

  These tests were controlled and carried out following this procedure:

  ✓ Activation of control panel

  ✓ Fan activation

  ✓ PCU HV-generator activation

  ✓ Recording test data

- Optimal operating potential for ES: a test was carried out to evaluate the electrical charge carried by liquid drops. For this purpose, a metallic mesh (f*ig. 4-24*) was installed under the ES units. The gas flow rate was set to zero, G = 0 m^3 / h and liquid flow rates were set at L = 1.568 m^3 / h and L = 1.872 m^3 / h, corresponding respectively to the spray pressure of 2 and 3 bar. The metallic mesh was connected to a tester (*ICE model 5200A*) in order to read current carried by the drops, sprayed by nozzles.

  These tests were controlled and carried out following this procedure:

✓ Activation of control panel

✓ Activation of compressor

✓ Activation of electrovalve

✓ Activation of supply pump

✓ Activation of PTV3 generator

✓ Recording test data

4.2.2 Experimental procedure for particle capture

Two campaigns were carried out:

❖ Test F
- G= 5500 m^3/h
- Dust flow = 2 kg/h
- Liquid flow, L= 5.535 - 7.821 - 9.594 m^3/h;
- V_{PCU}=13 – 15 – 16 kV
- V_{ES}=10 – 13 – 16 kV

❖ Test G
- G= 10000 m^3/h
- Dust flow = 2 kg/h
- Liquid flow, L= 5.535 - 7.821 - 9.594 m^3/h;
- V_{PCU}=13 – 15 – 18 kV
- V_{ES}=10 – 13 – 16 kV

These tests were controlled and carried out following this procedure:

1. Activation of control panel
2. Activation of Fan

3. Activation of compressor
4. Electrovalves opening
5. Activation of supply pump
6. Activation of generators
7. Activation of dust generator

   Particles are located in a tank. When the pump is active, they are withdrawn into a duct and collide against a plate *(Fig. 4-12).*

Figure 4-12 Air-dust suspension feeding system. 1- Supply tube; 2 - Collision plate

8. Particle capture tests. The abatement tests were carried out using a dust known as "Aramco Test Dust", composed of 90% of "Arizona Test Dust" and 10% of ground salt (mass percentage). There is also a rate of sodium chloride with a purity ranging from 99% to 100% (mass percentage). The chemical composition of Arizona Test Dust is shown in *Table 4-1*. Particle concentration is shown in *Fig. (4-13)* and obtained downstream the WES duct. It is important to highlight that the numerical concentration has to be multiplied for 100 because of the presence of the two diluters.

Chemical Ingredient	CAS Number	Percent of Weight
SiO_2	14808-60-7	68-76
Al_2O_3	1344-28-1	10-15
Fe_2O_3	1309-37-1	2-5
Na_2O	1313-59-3	2-4
CaO	1305-78-8	2-5
MgO	1309-48-4	1-2
TiO_2	13463-67-7	0.5-1.0
K_2O	12136-45-7	2-5

Table 4-1 Arizona test Dust Composition

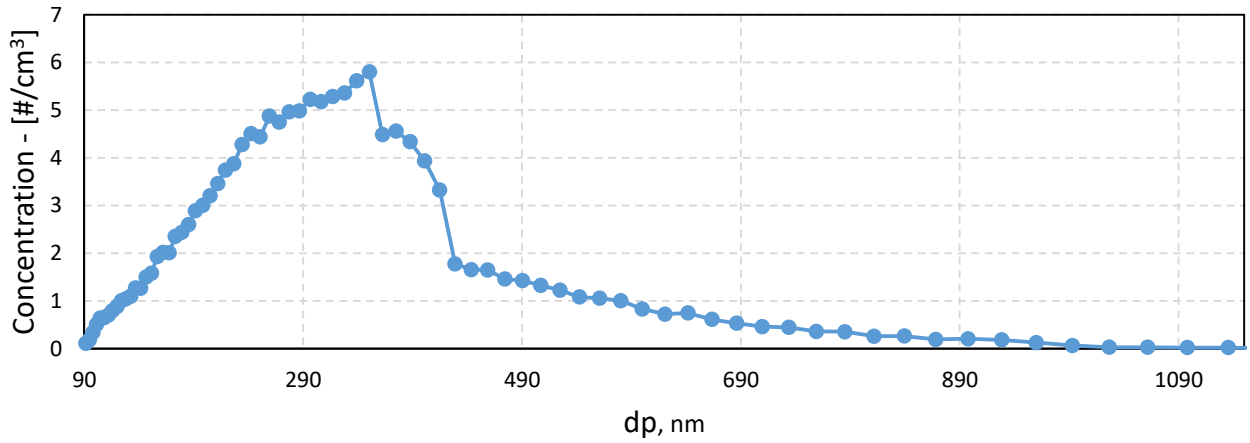

Figure 4-13 Arizona Dust Numerical Concentration

9. Particles are collected through a tube placed downstream the WES. With the two diluters (*Fig. 4-9*) it was possible to regulate the inlet gas flow, in order to respect the isokinetic between the main duct out the scrubber and the inlet tube of the analysis system. This operation in crucial for a such system because of the presence of ultrafine particles: the sample tube was placed exactly in the center of the outlet duct (in this way it was possible to avoid all the vortex and phenomena linked to the proximity of the wall) and the same velocity in the duct is forced to be present in the sample tube, in order to create the same fluid dyinamic conditions.

10. Sampling and recording data

The analyzer performs a certain number of samples, 20 seconds of duration each, depending on the total time of the test. For each sampling the instrument shows a row made up on numerical concentrations (N / cm^3), corresponding to particles different sizes (in nm). Referring to a specific granulometric class, the numerical concentration provided by the analyzer for each sampling is obtained by dividing the number of particles detected for the volume aspirated during the entire sampling (20 seconds). For example, *Table 4-2* represents the numerical

concentrations detected by the analyzer as a function of the sampling number (N^0_c) and the particle diameter (d_p). On the first row of the *Table 4-2* are shown the different particles diameters, while on the first column the sampling number is indicated.

	d_p, nm	91,52213	94,64665	97,88118	101,2257	104,6803	108,2547	111,9542	115,77375	119,72805	123,81761
N^0_c											
1		0,12119	0,060595	0,24238	0,24238	0,36357	0,908926	0,424165	0,5453554	0,4847603	0,3635703
2		0,060337	0,36202	0,120673	0,36202	0,36202	0,54303	0,663703	0,3016834	0,6637035	0,2413467
3		0,120644	0,241288	0,422255	0,422255	0,663543	0,663543	0,482577	0,1809664	0,7841876	0,3619327
4		0,180985	0,060328	0,301641	0,361969	0,301641	0,361969	0,422297	0,4222973	0,6032819	0,6032819
5		0,060309	0,120618	0,120618	0,723705	0,663397	0,542779	0,48247	0,542779	0,4221615	0,4221615
6		0,120564	0,301411	0,421975	0,361693	0,542539	0,421975	0,602821	0,482257	0,5425391	0,482257
7		0	0,120591	0,241182	0,602954	0,482364	0,422068	0,482364	0,6632499	0,9044317	0,3617727
8		0,060368	0,181105	0	0,482946	0,482946	0,482946	0,482946	0,7847872	0,6640507	0,6036825
9		0,060327	0,301635	0,422289	0,361962	0,784251	0,663597	0,663597	0,7239237	0,6635967	0,5429427

Table 4-2 Table shows the particulate concentrations recorded by the analyzer as a function of the sampling number (N^0_c) and the particle diameter (dp) for a certain gas stream

In order to evaluate the particle capture removal, four particle diameter values were chosen: d_p = 100 - 200 - 350 - 400 nm and at each diameter is associated the most probably concentration. These values are estimated taking into account the cumulative distribution function, obtained in correspondence of concentration values detected by analyzer for each particle size class. Only those cumulative distribution function included between 10% and 80% were considered. Four concentration are obtained with this method for each particle diameter.

4.3 Results and discussions

❖ *Test on PCU operating conditions*

These tests showed that the value of the discharge potential is equal to 21 kV for a gas flow rate of 5500 m^3 / h and 22 kV 10000 m^3 / h. *Table 4-3*.

Gas Flow, m^3/h	Humidity, %	Temperature, °C	Breakdown voltage, kV
5500	39.40	18	21
10000	47.23	19	22

Table 4-3 Operating conditions for PCU tests

❖ *Test on ES operating conditions*

This test was performed by 8 ES units switched on.

The results of experimental tests are shown in *Fig. 4-14a* and *4-13b*. *Figure 4-14b*, for the two liquid flows (L = 1.526 m^3 / h corresponding to 2 bar and L = 1.872 m^3 / h corresponding to 3 bar) spray current as function of applied voltage are presented. In *Fig. 4-14a* the values of the Droplet Charge to mass ratio (*D - CMR*) are shown.

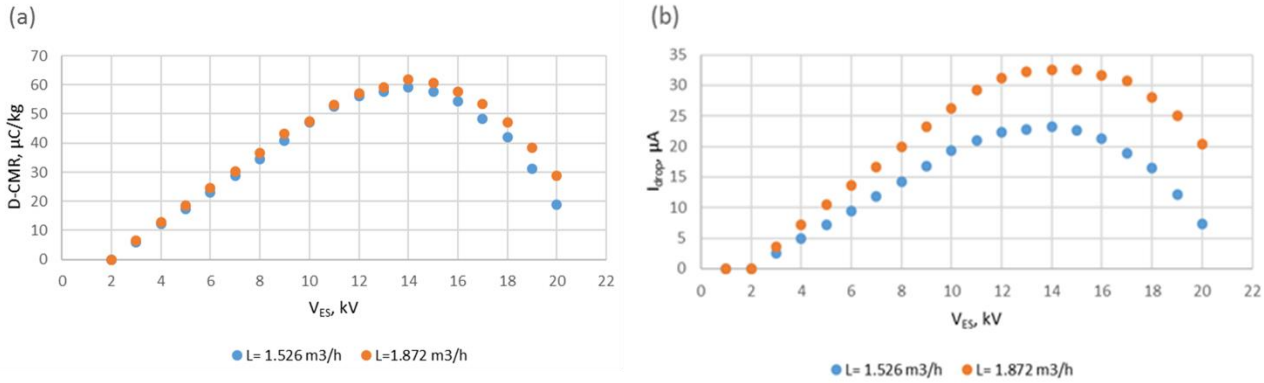

Figure 4-14 Droplet charge to mass ratio (a) and spray current (b) as a function of applied potential and parametric with the water flow rate

The trend is not monotonic: the D-CMR and spray current paths both show a linear growth up to a maximum value, above which the curve decreases reaching 0 at about 20 kV. The reason is to be

found in the various phenomena that take place during the charging phenomena that take place when drops are electrically charged through an induction system. In the first part, the charging mechanism is just inductive, therefore the droplets charge increases linearly with the applied potential. Once the maximum point is reached, due to the high potential, corona effect takes place.

Fig. 4-13b shows that the spray current value increases as the nozzle operating pressure increases. This fact is mainly due to the change in the morphology of the spray, which consists in the thinning of the liquid film that leads to an increasing of the surface area. Therefore, even pressure has its role in liquid layer morphology: increasing pressure on one hand, the liquid thickness decreases and liquid droplets are able to gain a higher charge, on the other hand the residence time of the drops is reduced in charging area, and so it is their exposure time to the electric field.

For our purpose, during the abatement tests, three potentials were used: 10 - 13 - 16 kV, respectively a value on the increasing branch of the D-CMR curve, one value at the maximum and a value on the decreasing branch of the curve, to understand how charging liquid phenomena of Liquid loading can affect the particle capture efficiency.

However, due to the high water flow rate, the tests carried out at the maximum flow rate corresponding to 3.9 l/ min for each nozzle, for a total of 9,594 m^3 / h were carried out only at the potential of 10 kV as electric discharge phenomena took place at potentials higher than this.

4.3.1 Particle capture tests

For G = 5500 m^3/h, nine different tests were performed by changing the PCU and the ES applied voltages (V_{PCU}, V_{ES}) and the water flow rate (L). *Table 4-4* shows the various operating conditions. In *Figure 4-15* shows the trend of capture efficiency ($\eta\ (d_p)$) as a function of the particle diameter (d_p). The results show that for the various operating conditions the abatement efficiency is always above 60%.

TEST	L (m^3/h)	V_{ES} (kV)	V_{PCU} (kV)
F_1	9,594	10	15
F_2	7,823	10	15
F_3	5,535	10	15
F_4	9,594	10	13
F_5	5,535	10	13
F_6	5,535	13	15
F_7	5,535	16	15
F_8	5,535	13	13
F_9	5,535	16	13

Table 4-4 Experimental conditions for F tests

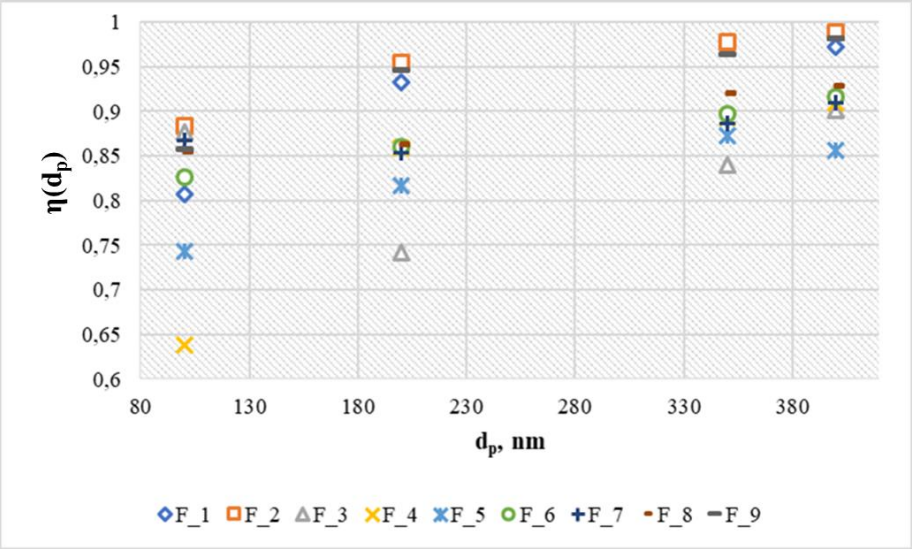

Figure 4-15 Capture efficiency vs diameter for Test F, obtained with "B" approach

For a higher gas flow rate, G = 10000 m^3 / h, nine tests were performed under different conditions belonging to the group called "Test G" (*Table 4-5*). The results obtained are shown in *Fig. 4-16* and

show the capture efficiency (η(dp)) as a function of the particle diameter (dp) of the aforementioned test.

TEST G	L (m^3/h)	V_{ES} (kV)	V_{PCU} (kV)
G_1	9,594	10	15
G_2	9,594	10	13
G_3	5,535	10	15
G_4	5,535	10	13
G_5	9,594	10	18
G_6	7,823	10	15
G_7	7,823	10	13
G_8	5,535	13	15
G_9	5,535	13	13

Table 4-5 Experimental conditions for G tests

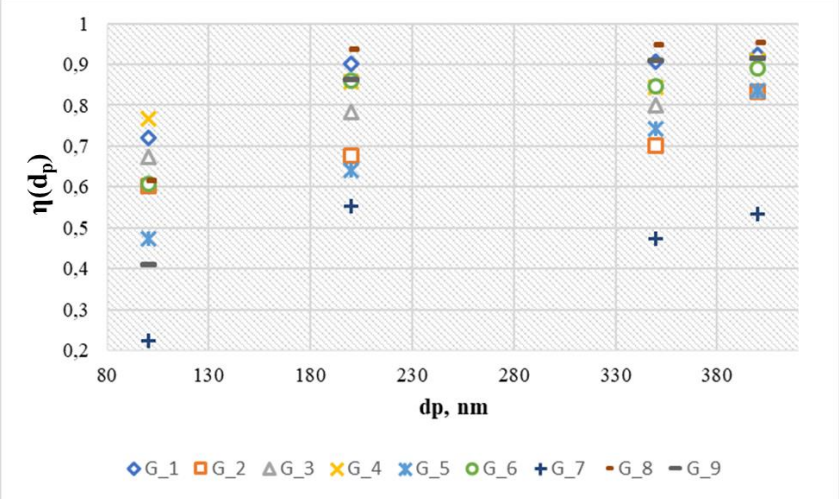

Figure 4-16 Capture efficiency vs diameter for Test G,

The best operating conditions are:

- G = 5500 m^3/h
- L = 9,594 m^3/h
- V_{ES} = 10 kV
- V_{PCU} = 15 kV

In terms of average capture efficiency for G = 5500 m^3/h, the experimental results are shown in *fig. 4-17*.

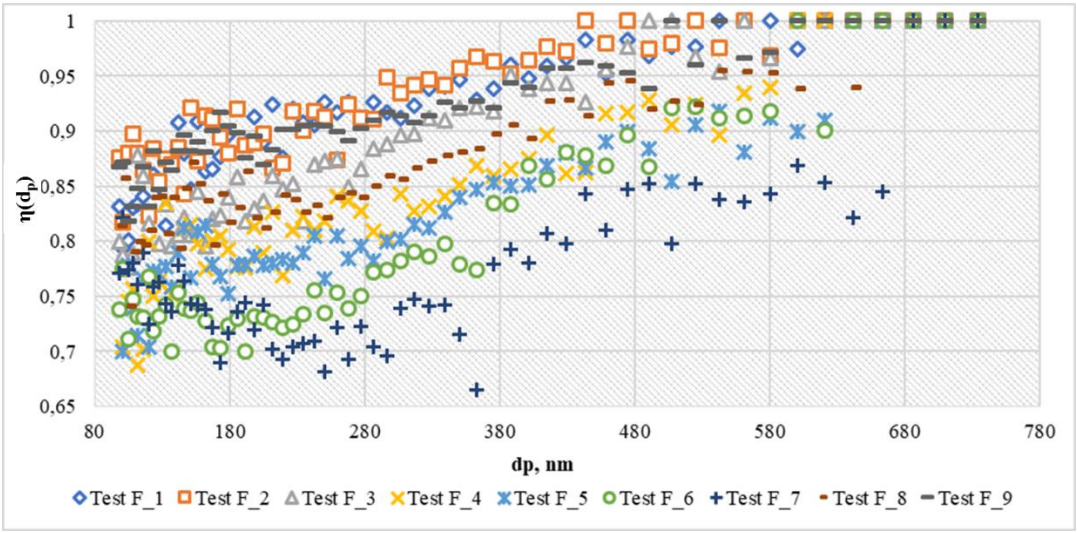

Figure 4-17 Capture efficiency vs diameter for Test F

The capture efficiency for the *F* tests has a minimum equal to 65% and in some cases overcome 99%.
For G = 10000 m^3/h the average capture experimental efficiency are shown in *Fig. 4-18*.

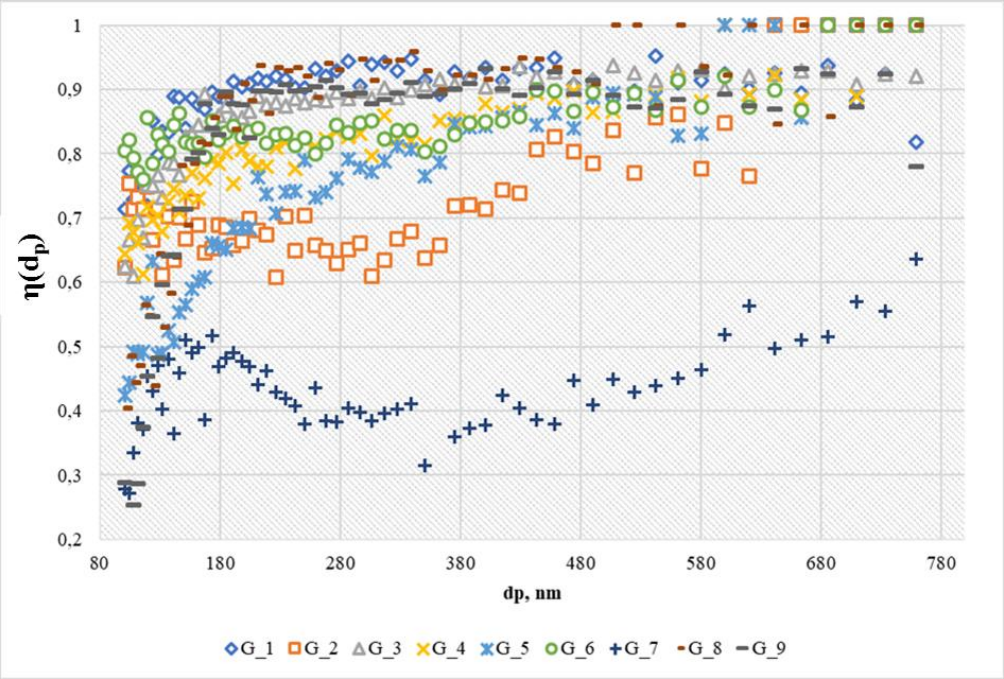

Figure 4-18 Capture efficiency vs diameter for Test G, obtained with "A" approach

The capture efficiency for the G tests is included in a range that has as lower value equal to 25% and as a higher about the unit.

4.3.2 Influence of operating parameters

In this section, all the parameters that influence the particle capture efficiency are compared.

- *Effect of PCU voltage*: increasing V_{PCU} from 13 to 15 kV, the particle capture efficiency increases as well (*Fig. 4-19*). The capture total efficiency for V_{PCU} = 13 kV is 84%, while for V_{PCU} = 15 kV is 93%.

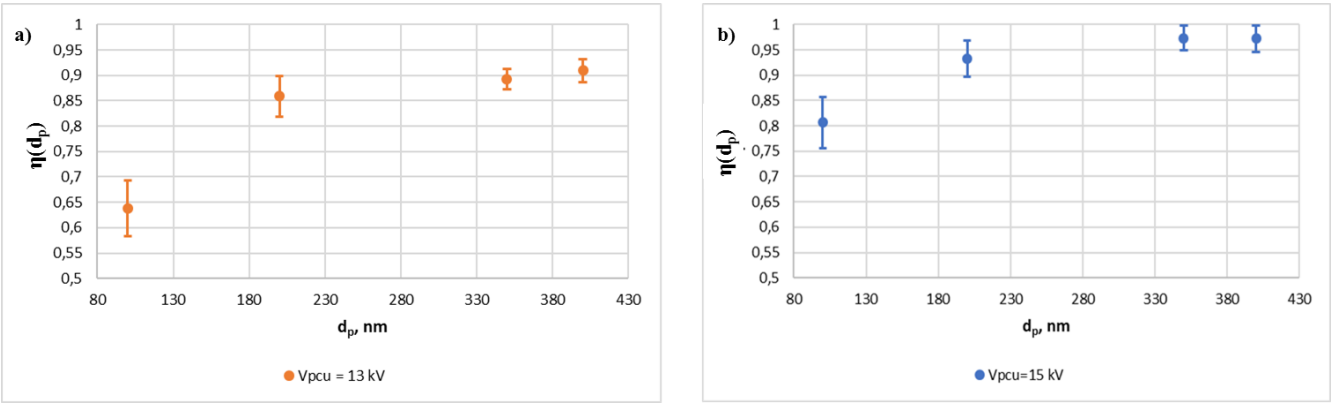

Figure 4-19 Comparison between particle capture efficiency, varying PCU voltage a) V_{PCU} = 13 kV b) V_{PCU} = 15 kV. Operating conditions: G = 5500 m^3/h, L = 9,594 m^3/h, VES = 10 kV

- *Effect of Liquid flow rate*: varying liquid flow L = 5,535 m^3/h - 7,823 m^3/h - 9,594 m^3/h and keeping the other variables unchanged, as shown in *Fig. 4-20*. The best operating conditions are shown when liquid flow is 9.594 m^3/h. Higher liquid flow rates are accompaigned by a higher density of sprayed droplets which obliosly lead to a higher removal efficiency. The removal efficiency at the three liquid flow rates are 83 %, 92 % and 95 % respectively.

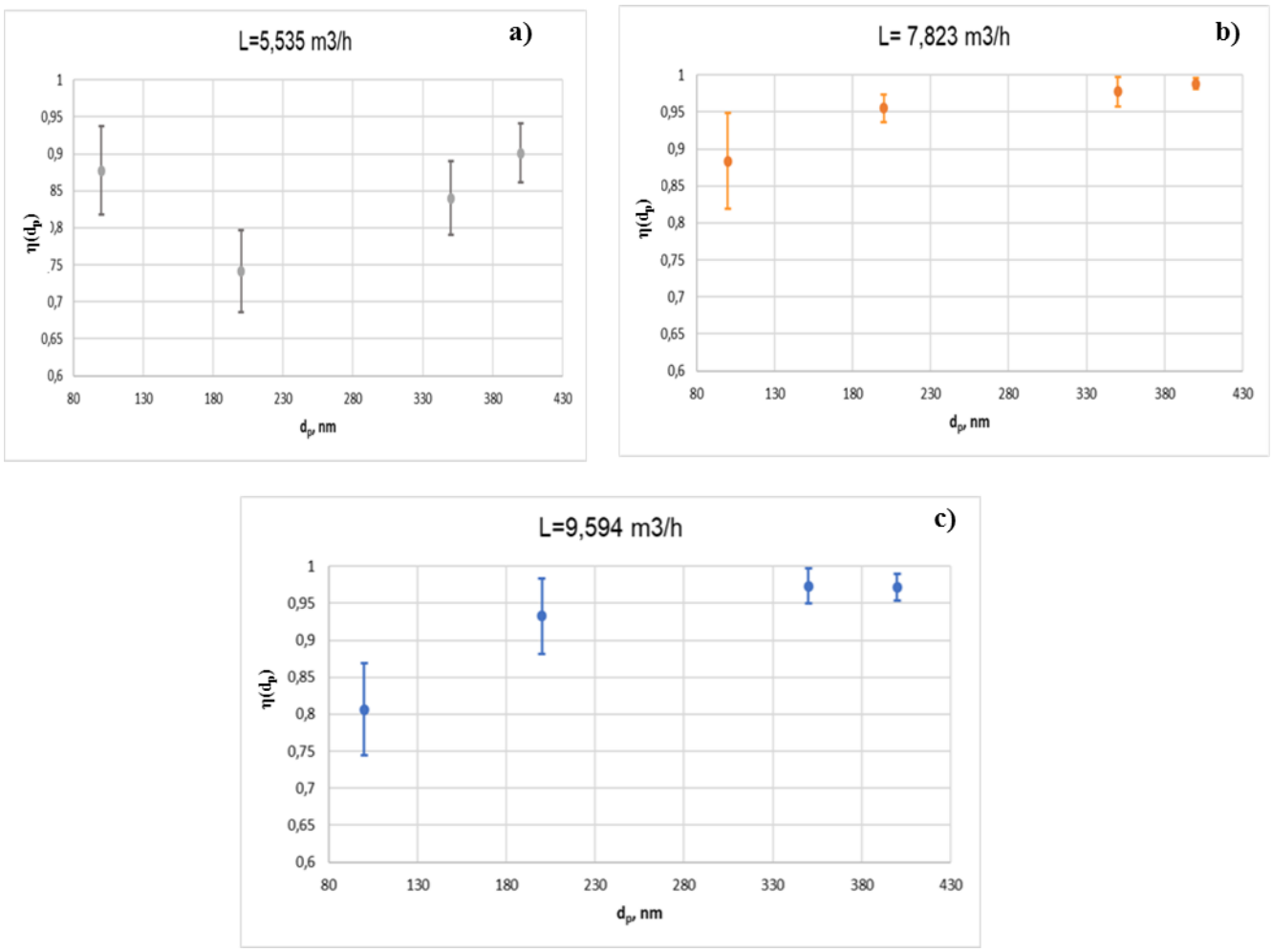

Figure 4-20 Comparison between particle capture efficiency, varying Liquid flow. a) L = 5.535 m^3/h b)L = 7.823 m^3/h c) L = 9.594 m^3/h. Operating conditions: G = 5500 m^3/h, V_{PCU} = 15 kV, V_{ES} = 10 kV.

- *Effect of the gas flow e:* increasing the gas flow rate from 5500 m^3/h to 10000 m^3/h, the capture efficiency decreases, as the gas residence time in the contact chamber decreases. Total capture efficiencies are 93 % and 85 % for G = 5500 m^3/h - 10000 m^3/h, respectively (*Fig. 4-21*).

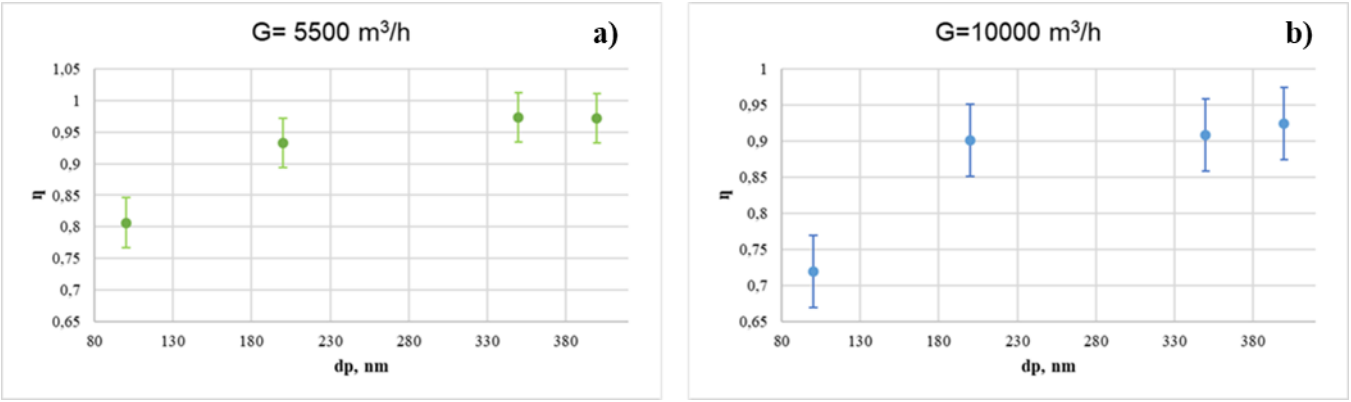

Figure 4-21 Comparison between particle capture efficiency, varying Gas flow. a) G = 5500 m^3/h b) G = 10000 m^3/h. Operating conditions: L = 9,594 m^3/h, V_{PCU} = 15 kV, V_{ES} = 10 kV

- *Effect of ES voltages:* it was not possible to make comparison among the three V_{ES} voltages because increasing the liquid flow rate, in particular at 9.594 m^3/h, setting a potential over 10 kV, there were arcs in ES devices, unwanted phenomena for this system. Therefore, the comparison was made fixing the liquid flow rate at the minim value (L = 5.35 m^3/h), with G= 5500 = m^3/h and V_{PCU} = 13 kV. Total capture efficiencies are 82 %, 91 % and 94 % for V_{ES}= 10 kV, V_{ES}= 13 kV and V_{ES}= 16 kV respectively (*Fig. 4-22*).

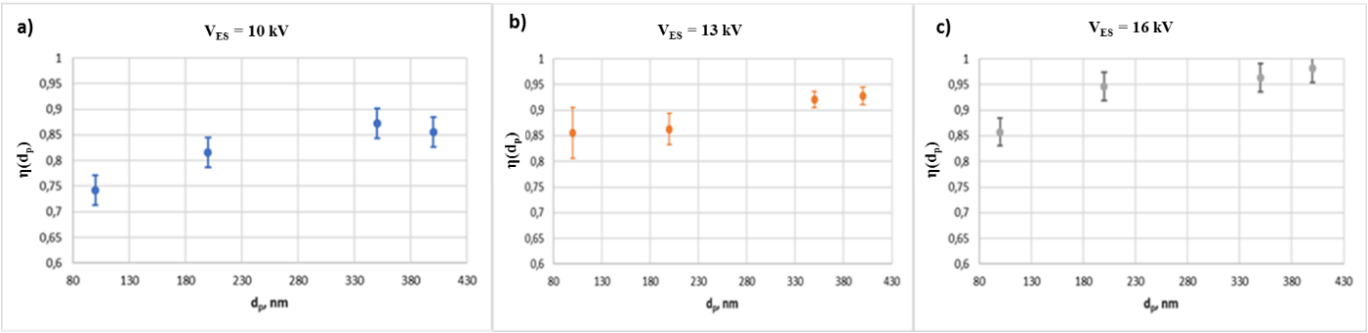

Figure 4-22 Comparison between particle capture efficiency, varying ES voltage. a) V_{ES} = 10 kV b) V_{ES} = 13 kV c) V_{ES} = 16 kV. Operating conditions: L = 5.35 m^3/h, V_{PCU} = 13 kV, G =5500 m^3/h

4.3.3 Comparison between Experimental and Modeled efficiency

Once obtained the experimental results, these data were compared to the PCD model described in *Chapter 3.3*. As previously presented, the empirical model shows different parameters with a certain error, but it was found out that the main uncertainties were due to the parameter *a* in the empirical formula (*eq. (4-1)*).

$$q(d_p)_{avg} = a \cdot d_p^b \cdot (V - V_0)^c \qquad (4\text{-}1)$$

Where

$a = 1.113 \cdot 10^{-8} \pm 4.68 \cdot 10^{-9}$

$b = 2.757 + 6.709 \cdot 10^{-2}$

$c = 7.308 \cdot 10^{-1} + 7.789 \cdot 10^{-2}$

In the new experimental conditions, the onset corona voltage, V_0, was equal to = 8 kV.

Applying the *eq. (4-1)* and comparing it with the experimental results, it was found out how the model predicts the experimental capture efficiency achieved during the tests at V_{PCU} = 15 kV. It is shown in *Figs. (4-23) and (4-24)* to the comparison between experimental and model results for both flow gas rates (5500 and 10000 m^3/h) at the higher liquid flow gas rate (L=9.594 m^3/h) and V_{ES} = 10 kV.

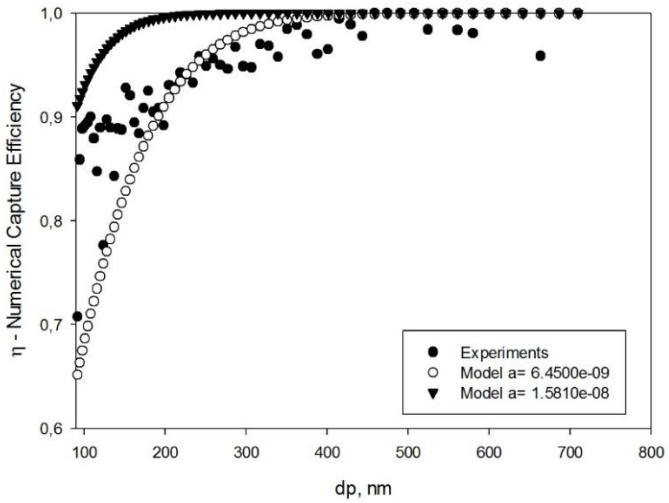

Figure 4-23 Comparison between experimental capture efficiency and particle efficiency evaluated applying the PCD model for particle charge. V_{PCU}= 15 kV, G=5500 m^3/h, L= 9.594 m^3/h, V_{ES} = 10 kV.

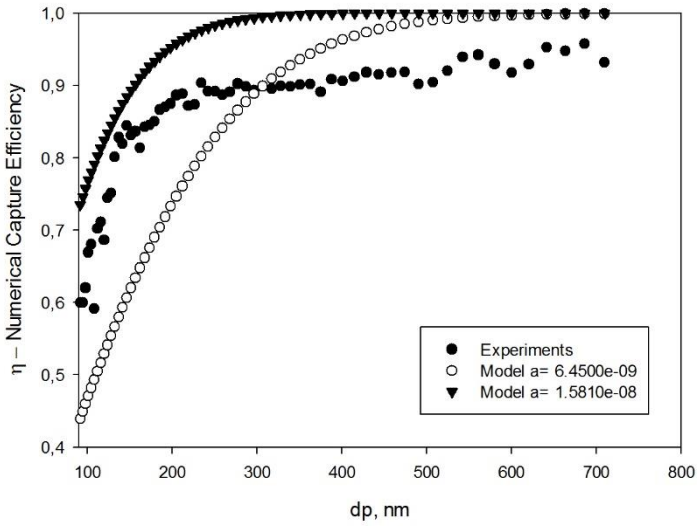

Figure 4-24 Comparison between experimental capture efficiency and particle efficiency evaluated applying the PCD model for particle charge. V_{PCU}= 15 kV, G=10000 m^3/h, L= 9.594 m^3/h, V_{ES} = 10 kV.

For G=5500 m^3/h the model is able to predict the numerical capture efficiency, while for G=10000 m^3/h the experimental data are lower compared to the model values. This result could be explained by the gas residence time that is lower for the higher gas flow rate, therefore a fraction of particles is not well treated.

Conclusions

The aim of this thesis was the analysis of particle capture in wet electrostatic scrubber (WES), with the final objective of design, build and operate the first prototypal unit for large flow rates (10.000 Nm^3/h), developed in collaboration with the Boldrocchi Ecologia s.r.l., which sponsored this Ph.D. activity.

WES is an emerging technology aimed at advancing the performance of conventional water scrubbers by improving gas absorption and particle capture rate. It combines the advantages of conventional spray towers with the effects of electrostatic interactions between particles and drops, therefore it is proposed as a valid alternative to other conventional technologies, such as electrostatic precipitators and sleeve filters, for the abatement of fine and ultrafine powders.

These improvements derive from the use of charged droplets and, optionally, from the exposure of the gas to a low-power corona source. Starting from several considerations on particle capture model, a deep literature study was carried on particle charging model through corona source. A reliable model to describe particle charging and consequently the particle abatement has been developed. A CFD simulation was proposed to model a set of experimental data available for an existing pilot scale device in order to obtain the fundamental parameters governing the scavenging model: the droplets distribution, their velocity along the reactor and the gas residence time. Once determined these parameters, we used the Wet Electrostatic Scrubber model to derive information on particle charging. In particular: two models were applied in post processing, the aerosol current (AC) model and the particle charge distribution (PCD) model. Applying the predictive model, there was not a good fitting between experimental and theoretical data and the reason is ascribable to the mean charge considered for each particle diameter. It was observed that at high PCU voltage, the AC model overrate the mean charge carried for particle diameter <200 nm, while underestimating the data for d_p > 200nm. Starting from experimental data, a suitable PCD model was developed to find the distribution of charges on a fixed particle diameter to obtain the established capture efficiency. The charge distribution has binomial shape that depends on a unique parameter *p* that is univocally determined through minimum square root for each particle size. The PCD allows to by-pass the mean charging estimation problems, showed by the AC especially for high PCU voltages. It attributes, on the basis of the experimental efficiency, the unique mean charge that allows the efficiency best fitting. It was demonstrated that the PCD model is consistent with experiments: at different liquid and gas flow rate and droplet charging conditions, provided that the particle charger,

the fitting parameter is almost the same. At the end of this study appears that a set of experiments is needed to understand all the theoretical lack showed by the AC model. An empirical formula of the average charge (evaluated as average value of a certain distribution of the PCD model) was obtained; a dependence on voltage and particle diameter was shown. This result allows to predict the operating conditions for new PCU devices with similar geometry.

This modelling results were used to size a new pilot scale unit of large size developed for the Boldrocchi s.r.l. (Italy). The Boldrocchi WES system was tested in a wide range of experimental conditions on a model test dust having size distribution mostly between 100 nm and 800 nm. The maximum numerical total capture efficiency (93%) is obtained for the following experimental conditions:

- G = 5500 m^3/h
- L = 9.594 m^3/h
- V_{ES} = 10 kV
- V_{PCU} = 15 kV

The experimental evidences are similar to those achievable with the best commercially available technologies, i.e. the fabric filters and the ESPs, but the lower pressure drops and the negligible effects of particle properties, i.e. electric resistivity or surface stickiness, suggest that the WES can be a valuable process in those conditions when fabric filters and ESP are not applicable.

The promising experimental results together with the theoretical background achieved during the thesis will be used to design an industrial WES plant as new technology for ultrafine particle abatement.

Bibliografy

[1] J. H. Seinfeld and S. N. Pandis, “Atmospheric Chemistry and Physics; From Air Pollution to Climate Change,” *Atmospheric Chemistry and Physics*. p. 1232, 1998.

[2] G. Oberdörster *et al.*, “Translocation of Inhaled Ultrafine Particles to the Brain,” *Inhal. Toxicol.*, vol. 16, no. 6–7, pp. 437–445, Jan. 2004.

[3] G. W. Penney, “Electrified Liquid Spray Dust-Precipitators,” 1944.

[4] “Best Available Techniques (BAT) Reference Document for the Production of Cement, Lime and Magnesium Oxide.”

[5] R. Remus, S. Roudier, M. a. Aguado Monsonet, and L. D. Sancho, *Best Available Techniques (BAT) Reference Document for Iron and Steel Production*, vol. BREF-IS. 2013.

[6] T. Lecomte *et al.*, “Best Available Techniques (BAT) Reference Document for Large Combustion Plants - Industrial Emissions Directive 2010/75/EU (Integrated Pollution Prevention and Control).”

[7] F. Di Natale *et al.*, “Capture of fine and ultrafine particles in a wet electrostatic scrubber,” *J. Environ. Chem. Eng.*, vol. 3, no. 1, pp. 349–356, Mar. 2015.

[8] L. D’Addio, F. Di Natale, C. Carotenuto, W. Balachandran, and A. Lancia, “A lab-scale system to study submicron particles removal in wet electrostatic scrubbers,” *Chem. Eng. Sci.*, vol. 97, pp. 176–185, Jun. 2013.

[9] W. G. N. Slinn, “Some approximations for the wet and dry removal of particles and gases from the atmosphere,” *Water. Air. Soil Pollut.*, vol. 7, no. 4, Apr. 1977.

[10] W. Licht, “Air pollution control engineering: Basic calculations for particulate collection,” 1988.

[11] D. S. Kim, D. Suk Lee, C. Gyu Woo, and M. Choi, “Control of nanoparticle charge via condensation magnification,” *J. Aerosol Sci.*, vol. 37, no. 12, pp. 1876–1882, 2006.

[12] C. H. Jung and K. W. Lee, “Filtration of Fine Particles by Multiple Liquid Droplet and Gas Bubble Systems,” *Aerosol Sci. Technol.*, vol. 29, no. 5, pp. 389–401, Jan. 1998.

[13] H. Davenport, L. P.-A. E. (1967), and undefined 1978, “Field studies of atmospheric particulate concentration changes during precipitation,” *Elsevier*.

[14] K. A. Nielsen and J. C. Hill, “Capture of Particles on Spheres by Inertial and Electrical Forces,” *Ind. Eng. Chem. Fundam.*, vol. 15, no. 3, pp. 157–163, Aug. 1976.

[15] J. F. Widmann, C. L. Aardahl, and E. J. Davis, “Observations of non-Rayleigh limit explosions of electrodynamically levitated microdroplets,” *Aerosol Sci. Tech.*, vol. 27, no. 5, pp. 636–648, 1997.

[16] A. Jaworek *et al.*, “Submicron particles removal by charged sprays. Fundamentals,” *J. Electrostat.*, vol. 71, no. 3, pp. 345–350, Jun. 2013.

[17] L. Manna, F. Di Natale, C. Carotenuto, and A. Lancia, “Electrified Water Sprays Generation for Gas Pollutants Emission Control,” *Chem. Eng. Trans.*, vol. 52, pp. 421–426, Aug. 2016.

[18] D. Xiao, “Fundamental Theory of Townsend Discharge,” Springer, Berlin, Heidelberg, 2016, pp. 47–88.

[19] W. S. Boyle and P. Kisliuk, “Departure from Paschen’s Law of Breakdown in Gases,” *Phys. Rev.*, vol. 97, no. 2, pp. 255–259, Jan. 1955.

[20] J. M. Meek, “A Theory of Spark Discharge,” *Phys. Rev.*, vol. 57, no. 8, pp. 722–728, Apr. 1940.

[21] L. B. Loeb, “Statistical Factors in Spark Discharge Mechanisms,” *Rev. Mod. Phys.*, vol. 20, no. 1, pp. 151–160, Jan. 1948.

[22] J.-S. Chang, P. A. Lawless, and T. Yamamoto, “Corona discharge processes,” *IEEE Trans. Plasma Sci.*, vol. 19, no. 6, pp. 1152–1166, 1991.

[23] C. E. Lapple, “Electrostatic Phenomena with Particulates,” *Adv. Chem. Eng.*, vol. 8, pp. 1–96, Jan. 1970.

[24] P. A. Lawless, “PARTICLE CHARGING BOUNDS, SYMMETRY RELATIONS, AND AN ANALYTIC CHARGING RATE MODEL FOR THE CONTINUUM REGIME,” 1996.

[25] J. Porteiro, R. Martín, E. Granada, and D. Patiño, “Three-dimensional model of electrostatic precipitators for the estimation of their particle collection efficiency,” *Fuel Process.*

Technol., vol. 143, pp. 86–99, Mar. 2016.

[26] Y. Zhuang, Y. Jin Kim, T. Gyu Lee, and P. Biswas, “Experimental and theoretical studies of ultra-fine particle behavior in electrostatic precipitators,” *J. Electrostat.*, vol. 48, no. 3–4, pp. 245–260, Mar. 2000.

[27] M. Pauthenier and M. Moreau-Hanot, “La charge des particules sphériques dans un champ ionisé,” *J. Phys. le Radium*, vol. 3, no. 12, pp. 590–613, 1932.

[28] N. A. Fuchs, “On the stationary charge distribution on aerosol particles in a bipolar ionic atmosphere,” *Geofis. Pura e Appl.*, vol. 56, no. 1, pp. 185–193, Sep. 1963.

[29] G. Biskos, K. Reavell, and N. Collings, “Unipolar diffusion charging of aerosol particles in the transition regime,” *J. Aerosol Sci.*, vol. 36, no. 2, pp. 247–265, Feb. 2005.

[30] D. R. A. McMahon, “The Boltzmann equation theory on charged particle transport.”

[31] H. J. White, “Electrostatic Precipitation Of Fly Ash,” *J. Air Pollut. Control Assoc.*, vol. 27, no. 1, pp. 15–22, Jan. 1977.

[32] R. C. Flagan and J. H. Seinfeld, “Of AIR POLLUTION ENGINEERING,” 1988.

[33] C. T. Crowe, T. R. Troutt, and J. N. Chung, “Numerical Models for Two-Phase Turbulent Flows,” *Annu. Rev. Fluid Mech.*, vol. 28, no. 1, pp. 11–43, Jan. 1996.

[34] “Chapter 19. Discrete Phase Models,” 2001.

[35] K. Yamada, “An empirical formula for negative corona discharge current in point-grid electrode geometry,” *J. Appl. Phys.*, vol. 96, no. 5, pp. 2472–2475, 2004.